

Article

# On the Magnetization and Entanglement Plateaus in One-Dimensional Confined Molecular Magnets

Javier I. Norambuena Leiva , Emilio A. Cortés Estay , Eric Suarez Morell  and Juan M. Florez \* 

Grupo de Simulaciones, Departamento de Física, Universidad Técnica Federico Santa María, Avenida España 1680, Valparaíso 2390123, Chile; emilio.cortes.ec@gmail.com (E.A.C.E.); eric.suarez@usm.cl (E.S.M.)

\* Correspondence: juanmanuel.florez@usm.cl

**Abstract:** One-dimensional (1D) magnetic systems offer rich phenomena in the quantum limit, proving more chemically accessible than zero-dimensional or higher-dimensional frameworks. Single-walled carbon nanotubes (SWCNT) have recently been used to encapsulate trimetric nickel(II) acetylacetonate [Nanoscale, 2019, 11, 10615–10621]. Here, we investigate the magnetization on spin chains based on nickel trimers by Matrix Product State (MPS) simulations. Our findings reveal plateaus in the exchange/magnetic-field phase diagram for three coupling configurations, showcasing effective dimeric and trimeric spin-ordering with similar or staggered entanglement across chains. These ordered states allow the qubit-like tuning of specific local magnetic moments, exhibiting disengagement or uniform coupling in entanglement plateaus. This behavior is consistent with the experimental transition from frustrated (3D) to non-frustrated (1D) molecules, corresponding to large and smaller SWCNT diameters. Our study offers insights into the potential of 1D-confined trimers for quantum computation, extending beyond the confinement of trimetric nickel-based molecules in one dimension.

**Keywords:** molecular magnets; entanglement entropy; matrix product states; magnetization plateaus



**Citation:** Norambuena Leiva, J.I.; Cortés Estay, E.A.; Suárez Morell, E.; Florez, J.M. On the Magnetization and Entanglement Plateaus in One-Dimensional Confined Molecular Magnets. *Magnetochemistry* **2024**, *10*, 10. <https://doi.org/10.3390/magnetochemistry10020010>

Academic Editor: Andrea Caneschi

Received: 28 December 2023

Revised: 23 January 2024

Accepted: 30 January 2024

Published: 1 February 2024



**Copyright:** © 2024 by the authors. Licensee MDPI, Basel, Switzerland. This article is an open access article distributed under the terms and conditions of the Creative Commons Attribution (CC BY) license (<https://creativecommons.org/licenses/by/4.0/>).

## 1. Introduction

The realization of quantum computation has found a promising playground on molecular magnetism [1]. Single-molecule magnets (SMMs) have garnered significant attention due to the unprecedented high-density information storage they offer, as well as to their quantum-tunneling of the magnetization [2], factorizing interactions [3] and a wide range of functionalizations that promise to improve the writing/reading in terms of computational times and decoherence [1,2,4]. The realization of molecular qubits [5] and phenomena such as quantum entanglement [6,7], optical/field control of spin dynamics, and molecular-gate-based quantum computation [8], in addition to magnetothermal effects [3,9,10], are already within reach.

Artificial SMMs can integrate multiple quantum resources and reduce the computational costs of certain applications [1,2]. Chemical design, guided by theoretical modeling and ab initio-based material informatics, allows further embedding of non-trivial quantum functionalities into each molecular unit, which could then act as a microscopic quantum processor capable of encoding error protected logical qubits or implementing quantum simulations [1]. Nevertheless, further scaling requires “wiring-up” multiple molecules, leading to a large Hilbert/Fock space and more complex degrees of correlation [5,11,12]. In this context, large-scale quantum computation would require suitable configurations of negligibly or slightly interacting molecular processors.

One-dimensional (1D) magnetic systems have been extensively studied over the last few decades because they are more chemically tractable compared to zero-dimensional systems and two- or three-dimensional frameworks [2,11,13,14] and are a rich source of new phenomena in the quantum limit, such as magnonic physics [15], Peierls instabilities [16],

Tomonaga–Luttinger liquids [17], and quantum phase transitions [18,19]. On the other hand, powerful methods for treating many-body systems such as Matrix Product States (MPSs) can work quasi-exactly in one dimension while allowing us to handle relatively large systems [20–22]; advances in digital experiments implementing these techniques and new paradigms based on variational quantum eigensolvers (VQE) in quantum chemistry [23] have prompted the search for new 0D–1D systems that can be realized in the nanoworld. Such low-dimensional systems could be formed from qudits, which provide more states to switch between compared to qubits [24,25], and multiple quantum states of diverse systems, including photons, trapped ions, impurity nuclear spins in semiconductors, embedded/encapsulated SMMs, and superconducting circuits [1,8,26] have already been used to exemplify feasible quantum units.

Here, we focus on 1D systems resulting from the coupling of several SMMs with quasi-one-dimensional exchange–interaction topologies that mimic their encapsulation by using carbon nanotubes, as recently achieved by Domanov et al. [26]. Encapsulation, embedding, and/or tailored confinement/deposition of molecular magnets is a cutting-edge path in SMM-based material prototypes [27–29] and, in particular, several Ni-based molecules have been synthesized from similar methods so far [26,30–32]. The aforementioned molecules revealed qualitatively different tunneling features from typical molecular magnets, such as  $\text{Mn}_{12}$  acetate or  $\text{Fe}_8$  [1,2,5]. For example,  $\text{Ni}_4$  has no tunneling in a zero magnetic field, and the electron paramagnetic-resonance EPR spectra exhibited unusual double sets of low-temperature peaks corresponding to slightly different easy magnetization axes [31]. Unlike  $\text{Mn}_{12}$  acetate and  $\text{Mn}_4$  dimer or  $\text{Fe}_x$  ( $x = 4, 8$ ), encapsulated Ni molecular magnets seemed not to be equally spaced from each other [31,33] and did not have effective giant spins. Furthermore, the couplings of Cr–Ni molecular rings were studied by using different ligand-transition metal bridges, and the different sizes of the ligands could tailor the intermolecular interactions in Ni-based molecules as well [32,34,35].

Additionally, the magnetization behavior of the spin-1 tetrameric  $\text{Ni}_4\text{Mo}_{12}$  molecule was studied within a post-Hartree–Fock approach, taking into account the contribution of delocalized electrons involved in complex exchange processes [36]. These contributions are favored when intricate exchange-bridge structures are present. Although such contributions are beyond the scope of this present study, they could be relevant within a framework that considers interactions between SMMs and the confining nanotubes' electronic degrees of freedom or focuses on other ferroic order parameters.

In this work, we study the encapsulation of trimetric nickel(II) acetylacetonate within a many-body approach, in which we effectively model the changes in the proximity of the molecular spins that result from being confined into a uni-axial arrangement, as it gives rise to the appearance of an intermolecular exchange interaction and to the quenching of the intramolecular exchange.

The intermolecular interaction is modulated within a framework that considers three different arrangements of molecules inside the nanotubes, and the intramolecular interaction ranges between the values of the so-called 3D and 1D systems, associated with the different diameters of the nanotubes in the experimental results, i.e., 2.1 and 1.3 nm, respectively [26]. Using MPS simulations, we characterize the magnetization of the resulting spin chains and their entanglement entropy, paying particular attention to the presence of magnetization plateaus and their response to the application of a magnetic field.

The presence of magnetization plateaus in magnetic systems is a fingerprint of, for example, quantum-level crossing and spin tunneling [35,37], competing metastable states in triangular-lattice arrangements of one-dimensional chains [38], geometrically frustrated layered systems [39,40], factorizing fields in coupled trimers [3], and effective spin fractionalization in spin trimer chains [10,12,27].

Through the analysis of the plateaus, we show the existence of effective dimeric and trimeric spin orders formed by intermolecular neighboring spins. Such orders possess constant/staggered entanglement for specific ranges of magnetic fields at which local

magnetic moments can be tuned in a qubit-like manner; effective dimers or trimers are either disengaged or uniformly coupled in such entanglement plateaus while protecting the tunable spins. These results can provide further insights into the potential of the different effective 1D confined trimers for quantum computation.

This work is organized as follows: In Section 2, we describe the molecular models and the quantum methods that were used. In Section 3, an overview of the general exact solution for the coupling of two molecules is presented. In Section 4, the MPS solutions for the ground state properties, such as local/total magnetization and entanglement entropy corresponding to the aforementioned spin chains, are discussed for a series of magnetic fields, coupling parameters, and number of molecules. Section 5 presents the conclusions of this work.

## 2. Trimetric Ni-Based Single Chain Magnets and Quantum Methods

This section describes the many-body magnetic model for the spin chains constructed by coupling the trimetric SMMs described in the work of Domanov et al. [26]. Typical SMMs have the coordination of supramolecular complexes consisting of a magnetic core surrounded by a shell of organic ligand molecules [35]. In Domanov's work, they initially use molecules in which there are no atomic bridges between molecules in the crystal lattices, and the closest transition metals are sufficiently distant so that intermolecular spin–spin couplings, due to both exchange and dipolar interactions, are expected to be negligible. However, this trimetric nickel(II) acetylacetonate [41] experienced a modulation of their intramolecular interactions when encapsulated in carbon nanotubes of different diameters [26]. Such modulation from a 3D- to 1D-like molecule turned from a frustrated behavior to a non-frustrated state in which all the exchange couplings were partially quenched, while the inter/intramolecular distances and local spin centers also changed.

The encapsulation of magnetic molecules within carbon nanotubes has been shown to lead to intermolecular interactions in similar systems [42]. A full chemical description of nickel(II) acetylacetonate units can be found in the references [26,41,43].

### 2.1. Spin Chains: Hamiltonian Modeling

Figure 1 displays the trimetric molecules used to form the spin chains. The differences between the 3D and 1D SMMs are due to the full quenching of the coupling  $J_{13}$  between two of the Ni ions (1 and 3 in Figure 1), which end up antiferromagnetically sharing the “central” Ni while breaking the triangular symmetry for the smaller nanotube diameters; the symmetric exchange coupling between the central Ni and its two nearest-neighbors, i.e.,  $J_{12}$  and  $J_{23}$ , are initially ferromagnetic, giving rise to a frustrated-like state for comparatively larger nanotube dimensions [26].

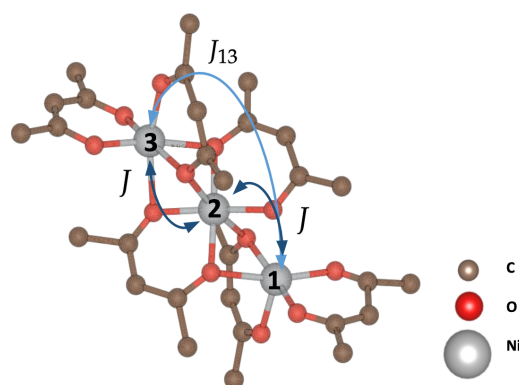


**Figure 1.** 3D trimetric nickel(II) acetylacetonate ( $\text{Ni}(\text{acac})_2$ ) (H atoms are not shown for sake of simplicity). The spins of nickel ions are superexchange-coupled through oxygen ligands, with exchange constant  $J_{12,23}$  between the nearest-neighbor spins and  $J_{13}$  between the terminal spins [26].

We then connected the trimers by simulating the three one-dimensional-like exchange topologies that are depicted in Figure 2. We considered the SMMs just close enough so that the two closest spin centers between the nearest-neighbor (which are abbreviated as “nn” from now on) molecules could interact while also considering a suitable distribution along the nanotube, i.e., other Ni ions belonging to those nn molecules were always separated by larger ligand distances.

The three configurations considered within this scope, labeled as “linear” (*L*), “alternated” (*A*), and “perpendicular” (*P*) are, respectively, shown in Figure 2a–c. In the *L* configuration, the Ni ions are assumed to be closely aligned along the axis of the nanotube; in the *A* case, one molecule is arranged along the axis and the second along the nanotube diameter; in the *P* case, the two sets of molecular spins are oriented perpendicular to each other in two parallel planes transversal to the nanotube. Figure 2d displays a schematic of the Ni(acac)<sub>2</sub>-filled SWCNTs (single-wall carbon nanotubes) as the SMMs are being wrapped. To model the precise arrangement of the SMMs inside the SWCNTs would likely require a mixture of experimental, ab initio, and/or Hamiltonian techniques; however, there have been only a limited amount of approaches to form ordered structures inside the nanotube channels [26,42], and recent experiments with magnetic molecules still lack enough insight on this particular inquiry [44]. In this work, we explore three of the highest-symmetry configurations with respect to the axis of the tube and the planes perpendicular to it, which could be used to screen and/or interpret other energetically stabilized molecular arrangements.

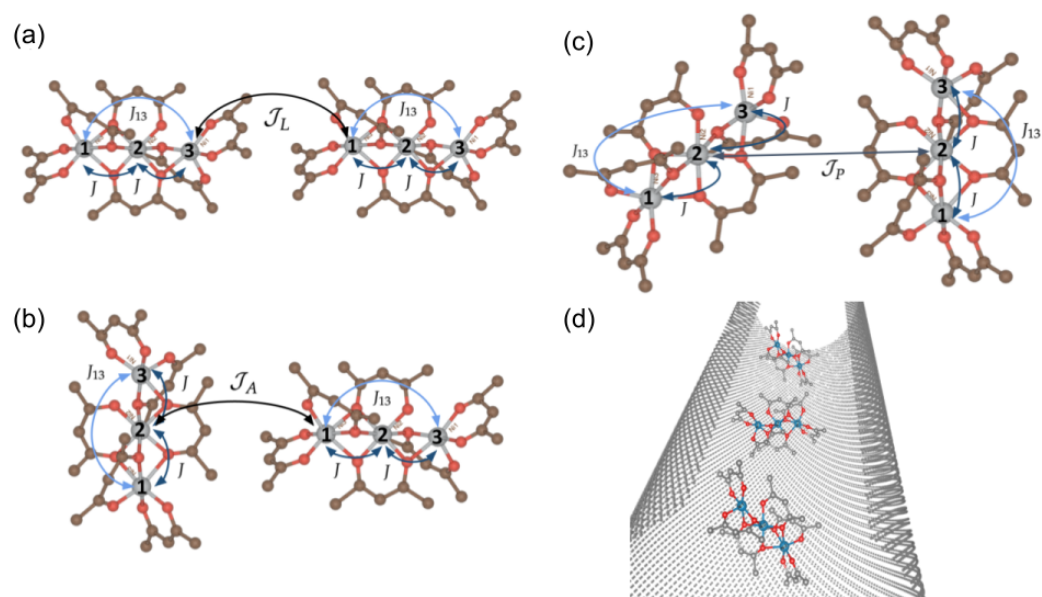


**Figure 2.** Nearest-neighbor Ni-trimers conforming the molecular chains; three types of exchange interactions are considered to couple the single magnets in Figure 1, i.e., “linear”  $\mathcal{J}_L$  (a), “alternated”  $\mathcal{J}_A$  (b), and “perpendicular”  $\mathcal{J}_P$  (c). (d) Single-wall nanotube-confined trimers, which give rise to molecular spin chains described by Equation (1).

The intermolecular exchange couplings associated with the aforementioned configurations follow the (*L*, *A*, and *P*) subscript notation from now on. Equation (1) describes the Hamiltonian model that accounts for the magnetic interactions in the resulting single chain magnets as modeled in this work:

$$H_{L,A,P} = \sum_{i=1}^N [H_i^{SM} + H_i^{Local}] + H_{L,A,P}^{Chain}, \quad (1)$$

where  $H_i^{Local} = -\mu_B g h \sum_{j=1,i'}^3 S_{j,i'}^z$ ,  $h$  corresponds to the magnitude of the external magnetic field,  $g = 2$  is the gyromagnetic factor [26],  $\mu_B$  is the Bohr magneton, and  $H_i^{SM}$  is presented in Equation (2), such that for each of the N SMMs added to the chain we have

$$H_i^{SM} = -2J(S_{1,i} \cdot S_{2,i} + S_{2,i} \cdot S_{3,i}) - 2J_{13}(S_{1,i} \cdot S_{3,i}). \quad (2)$$

The non-local ( $L$ ,  $A$ , and  $P$ ) interactions are represented by  $H_{L,A,P}^{Chain}$ , where the sum in Equation (3) is carried out so that we have open boundary conditions.

$$H_{L,A,P}^{Chain} = - \sum_{i=1}^{N-1} \mathcal{J}_{L,A,P} (S_{(3,2,2),i} \cdot S_{(1,1,2),i+1}) \quad (3)$$

In Equation (2),  $J = J_{12} = J_{23} = 1.49x$  meV, with  $x = 1$  corresponding to the 3D Ni(acac)<sub>2</sub> case with a ferromagnetic superexchange coupling between (1,2) and (2,3) local nickel atoms, and  $J_{13} = -0.89y$  meV, with  $y = 1$  representing the antiferromagnetic superexchange between (1,3) local molecular spins [26]. Also,  $\mathcal{J}_L = \mathcal{J}_{31}$ ,  $\mathcal{J}_A = \mathcal{J}_{21}$ , and  $\mathcal{J}_P = \mathcal{J}_{22}$ , where the subscripts refer to two nn molecules, respectively. Note the difference between the intra ( $J$ ) and intermolecular ( $\mathcal{J}$ ) couplings and that ( $x, y$ ) are parameters that allow us to follow the differences between the experimental exchange interactions and those simulated here, which, without loss of generality, could represent other molecular systems. In addition, the local magnetic moments for nickel are considered to have originated on a 3D shell with two unpaired electrons, i.e.,  $S = 1$ , as suggested in several previous results [26,33,41].

## 2.2. Quantum Many-Body Methods: DMRG and MPS

To investigate the ground-state (“gs” from here on) properties of finite-length molecular chains, as modeled in the previous section, we use MPS to represent the quantum states of the spin chains  $|\psi\rangle = \sum_{\mathbf{s}} c^{s_1 \dots s_N} |s_1 \dots s_N\rangle = \sum_{\mathbf{s}} A_1^{s_1} \dots A_N^{s_N} |s_1 \dots s_N\rangle$  ( $A_i^{s_i}$  factorizing matrices) and employ density-matrix renormalization group (DMRG) techniques to reach such gs [45]. DMRG has been successfully used in the investigation of, e.g., magnetization plateaus and excitations in spin-1/2 chains [27] and antiferromagnetic spin-1/2 molecular clusters in caged geometries [46], as well as in chains of coupled trimers [10] and mixed spin-(1/2,5/2,1/2) chain models [47]. Moreover, matrix representations make it suitable for the implementation of powerful time-evolving algorithms; for instance, time-dependent variational principle (TDVP) [48,49] or time-evolving block decimation (TEBD) [50]. However, the time-dependent properties of Ni-based spin chains are outside our scope but will be researched elsewhere.

Our simulations employ MPS and DMRG algorithms implemented in the Tensor Network Python (TeNPy) package [51]. In this framework, we allow a maximum bond dimension of  $\chi = 3200$  and consider our calculations converged within/below successive energy differences of  $10^{-12}$  [45,51].

As we will show in the next sections, representative magnetic/entanglement properties are extracted from spin chains formed by 6–12 trimers, i.e., 18–36  $S = 1$  local spin sites. Such systems represent a Hilbert space dimension that is too large to perform full diagonalization, unpractical for analytical methods that could solve specific parts of the configurational space considered here [31] and difficult to treat using Monte Carlo methods due to the local and clustered frustrations present here [12,38,39].

On the other hand, entanglement entropy, along with related measures such as quantum concurrence and mutual information, have become widely employed for assessing the entanglement characteristics of complex many-body systems [6,52,53]. Various studies have utilized these measures, exploring entanglement dynamics in confined spin chains [54], examining the localization of nuclear spin chains [55], and observing phase transitions in the spin-1 Heisenberg model through tripartite entanglement [56]. Additionally, investigations into bipartite entanglement have been conducted in tetranuclear Nickel complexes [33].

The quantification and measurement of entanglement extends to diverse methods, such as neutron scattering in quantum magnets [57] and many-body interference in ultracold atoms [6].

In this work, in addition to local and total magnetization, we also show the behavior of the entanglement entropy or von Neumann entropy ( $S$ ) [58] as a function of the system parameters. This  $S$  quantifies the entanglement between two subsystems of the chains [53,59]. We have chosen to divide each chain into two parts, depending on the particular site/bond being analyzed, with those two being called  $A$  or  $B$ , respectively. The entanglement entropy is then calculated from the reduced density-matrix  $\rho_A$  of subsystem  $A$  (or  $\rho_B$  for  $B$ ) according to

$$S = -\text{Tr}(\rho_A \ln \rho_A), \quad (4)$$

with  $\rho_A = \text{Tr}_B(\rho_{AB})$  (or  $\rho_B = \text{Tr}_A(\rho_{AB})$ ). We then use  $S$  to obtain further insight into the spin chain magnetization behavior and to study the ground-state characteristics according to the different intermolecular and intramolecular couplings that could be occurring with the confinement of the molecules.

### 3. 3D and 1D Molecular Magnets

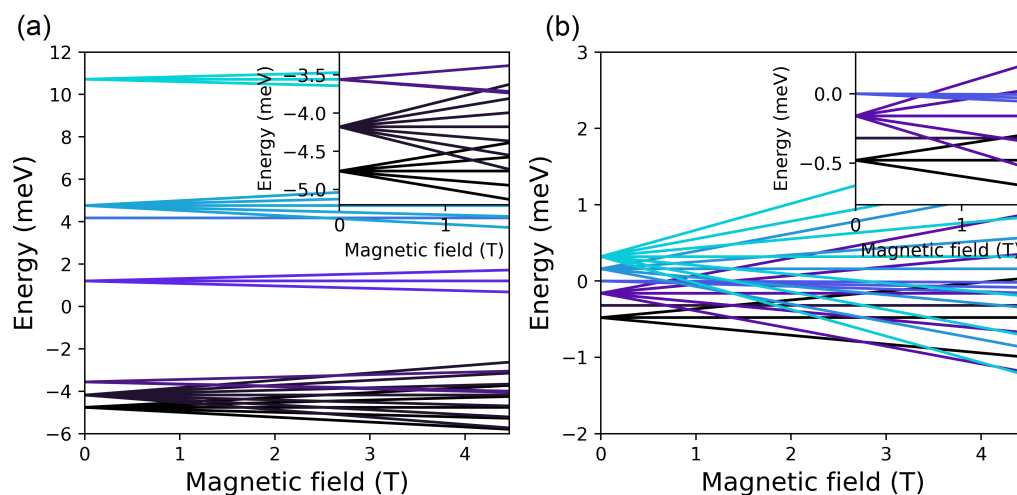
In this section, we present the quantum properties of the so-called 3D and 1D single molecules and the solutions for two coupled molecules. Although we focus on the chain magnets, the solutions in this section will allow us to have an intuition about the magnetization and entanglement responses to the confinement-promoted interaction between several molecules. Finite-temperature solutions for the magnetization are also presented in this section for discussion purposes regarding the thermal stability of the finite-size magnetization plateaus. However, our chain magnet MPS simulations are performed without considering the thermal effects.

#### 3.1. SMM Solutions

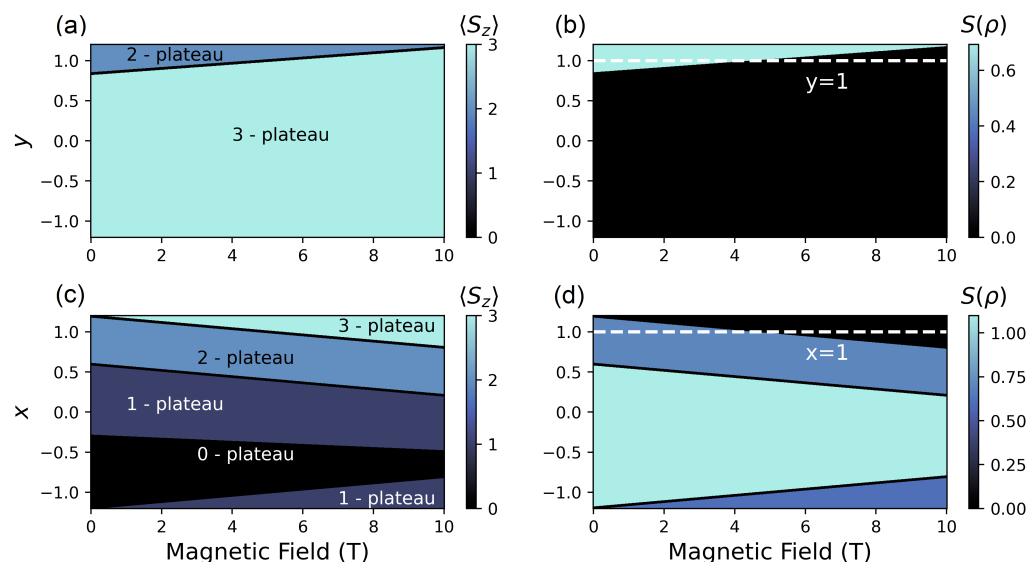
Figure 3 displays the exact energy eigenvalues of Equation (2) plus the Zeeman term ( $H_i^{\text{Local}}$ ) for  $(x = 1, y = 1)$  and  $(x = -0.0537, y = 0)$  corresponding to the single 3D and 1D molecules, respectively. The lower-energy states appear in the insets of Figure 3, having  $S_{i\text{-th}}^z = (2, 1, 0, -1, -2)$  ( $i$ th isolated molecule) in the case of 3D (lowest five) and  $S_{i\text{-th}}^z = (1, 0, -1)$  for 1D (lowest three), correspondingly. For the global ground-state in 3D, where the large ferromagnetic  $J$  (60% larger than  $J_{13}$ ) dominates promoting pairwise ferromagnetism (FM) between  $S_{(1,i),(2,i)}$  and  $S_{(2,i),(3,i)}$ , providing us with larger  $S^z$  projections than the 1D case, where the spins have an evenly promoted antiferromagnetism (AFM) in either spin pair. Hence, local frustrations are satisfied in the subset states due to nn AFM spins ( $S_{(1,i),(2,i)}$  or  $S_{(2,i),(3,i)}$ ) or the resulting local  $S_{j\text{-th}}^z = 0$ . In Appendix A, we have listed all the analytical eigenstates associated with the above energy spectra.

Figures 4 and 5 show the behavior of the magnetization and entanglement entropy of 3D and 1D SMMs as a function of the scaled experimental exchange interactions and the magnetic field, respectively. Comparing Figure 4a,c we see that  $J_{13}$  provides the SMM with a large magnetization for small magnetic fields, independent of whether it has either an AFM or FM nature, while  $J$  allows the system to reach small magnetizations for AFM values and larger ones for FM cases but requires a large magnetic field to saturate the system. The plateaus in this paper are represented by constant magnetization/entanglement values for the system's response to certain magnetic fields and/or along the chain sites/bonds for specific fields/exchange values.

Figure 4b,d shows that the 3D SMM is above a minimal entanglement phase diagram region, where polarized states contribute to the "3"-plateau, and a small decrement of  $J_{13}$  can quench the entropy while the magnetic field accelerates the appearance of such a region. On the other hand,  $J$  promotes regions of larger entropies as more solutions for a specific total  $S_z$  are possible by using different single-site states. Such regions exhibit a lower magnetization compared to the  $x = 1$  line in Figure 4d.



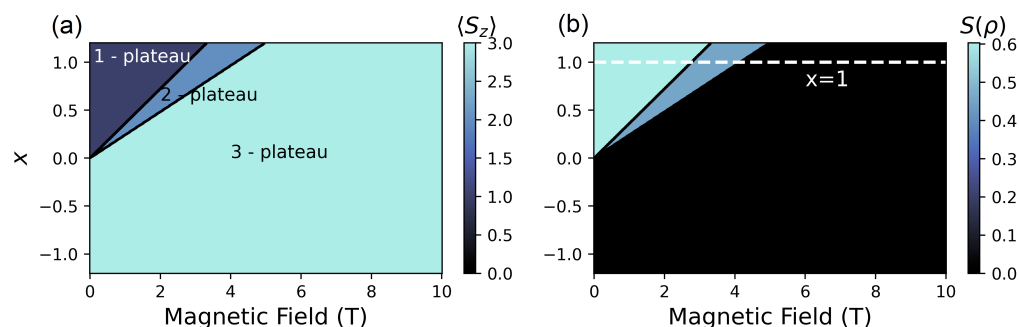
**Figure 3.** Energy levels of 3D (a) and 1D (b) trimetric nickel(II) acetylacetonate ( $\text{Ni}(\text{acac})_2$ ) [26]. Here, 3D corresponds to  $(x = 1, y = 1)$ , whereas 1D corresponds to  $(x = -0.0537, y = 0)$  according to notation in Section 2.1. Colorful lines are for visualization purposes respect to the field-driven breaking of energy degeneration.



**Figure 4.** Three-dimensional SMM magnetization along the field (a,c) and von Neumann entropy (b,d) as a function of  $y$  with  $x = 1$  (a,b) and of  $x$  with  $y = 1$  (c,b). We have used the notation “ $S_z$ ”-plateau to refer to the characteristic constant magnetization of the respective plateaus.

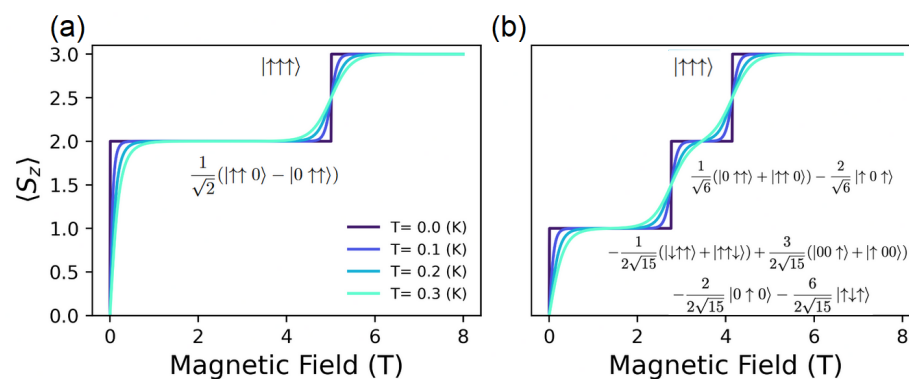
$S(\rho)$  in Figure 4 has been evaluated for the bond between spins 1 and 3, with the molecular dominant states given by  $\frac{1}{\sqrt{3}}(-|0 \uparrow 0\rangle + |\downarrow \uparrow \uparrow\rangle + |\uparrow \uparrow \downarrow\rangle)$  and  $\frac{1}{\sqrt{6}}(-|0 \downarrow \uparrow\rangle + |0 \uparrow \downarrow\rangle + |\downarrow 0 \uparrow\rangle - |\downarrow \uparrow 0\rangle - |\uparrow 0 \downarrow\rangle + |\uparrow \downarrow 0\rangle)$ , respectively. If we use the notation given by Ginsberg [41] for the total and  $z$ -projected magnetization, these correspond to  $(1, 0)$  and  $(0, 1)$ , which means that the magnetization difference between these two depends on the central  $S_{(2,i)}$  that we are tracing out, and we are left with the same total  $S_z$  for spin pairs 1–3 as the entanglement entropy in Figure 4d shows.

Figure 5 for the 1D SMM shows that the AFM intramolecular couplings enrich the phase diagram with more magnetization plateaus as a consequence of both the frustration and competing factorizing fields that are no longer boosted by the  $J_{13}$  exchange; this, in turn, extends the zones for finite entanglement entropy but slightly decreases the entropy at each plateau (except the “3”-plateau) as spins 1–3 are not directly coupled anymore.



**Figure 5.** One-dimensional SMM magnetization along the field (a) and von Neumann entropy (b) as a function of  $x$  with  $y = 0$ .

The magnetization plateaus of 3D ( $x = 1, y = 1$ ) and 1D ( $x = -0.0537, y = 0$ ), and the lowest-energy states associated with them, are depicted in Figure 6 for different values of temperature. According to these figures, the first magnetization plateaus as a function of the increasing magnetic field are robust against the temperature; they are also wider when the spins  $S_{(1,i),(3,i)}$  interact directly as in 3D, with larger fields required to reach the same magnetization in the absence of such interaction. Therefore, having more plateaus before saturation (more suitable if we were to look for switchable properties at lower fields) is possible in the 1D SMM in contrast to the 3D one. This figure also suggests that shorter plateaus (1D in this case) in systems with more molecules could be thermally wiped out or easily switched by the field, for which not all the plateaus are to be of interest. Therefore, nanostructures formed from these two SMMs, which could to some extent display all these properties combined, are interesting, and such is the case of the Ni(acac)<sub>2</sub>-filled SWCNTs simulated here.



**Figure 6.** Robustness of magnetization plateaus under different temperatures in (a) 3D and (b) 1D structures. In the 3D structure, the switching occurs around 5 (T); meanwhile, in the 1D structure, it occurs around 2.76 and 4.15 (T).

In Figure A1, we compare our results with experimental data from Ref. [26], finding good agreement with the magnetic behavior at the temperature of 5 K at which the experiment was carried out. This figure also suggests that for observing magnetization plateaus in the experimental measurements, temperatures below 1 K and/or higher magnetic fields would be required.

### 3.2. Two Coupled Molecules

We now couple two 3D or two 1D SMMs according to the configurations described in Section 2 and focus on finding a phase-space region (formed by the strength of the exchange interactions and the magnetic field) where the many-body calculations could extract representative information. The magnetization as a function of the magnetic field for the three different couplings, i.e., with  $\mathcal{J}_L$ ,  $\mathcal{J}_A$ , and  $\mathcal{J}_P$  are displayed in Figure 7.

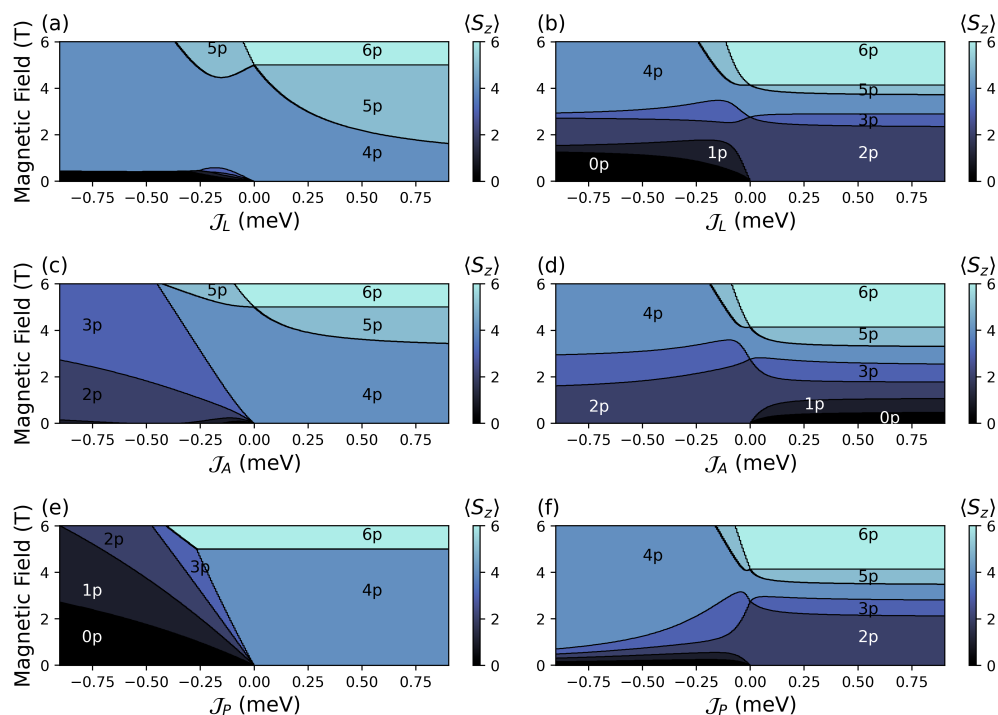


**Figure 7.** Magnetization phase diagrams corresponding to  $\mathcal{J}_L$ ,  $\mathcal{J}_A$ , and  $\mathcal{J}_P$  configurations for the 3D molecules (a,c,e) (left column) and 1D ones (b,d,f) (right column), respectively.

The magnetization plateaus for a selection of exchange couplings are displayed in Figures A2 and A3. In Figure A4, the phase diagrams for the entanglement entropy are presented as well. Figure 7 shows that the configuration of the coupling between the nn SMMs is crucial to the landscape of the plateaus (for simplicity, from this point on, we abbreviate the “#”-plateau as “#p”). The plateaus appear distributed over a wide range of magnetic fields/coupling strengths and are associated with several magnetization values with a staggered-like behavior and  $\langle S_z \rangle$ -jumps for varying magnetic fields.

From our scope, the main characteristics to be pointed out in the magnetization diagrams of Figure 7 are the following: in the 3D case, the FM couplings favor larger magnetization plateaus when spins  $S_{(1,i)}$  and/or  $S_{(3,j)}$  are involved; the AFM couplings favor larger magnetization plateaus if spin-2 interactions are not involved. For the  $\mathcal{J}_L$  configuration, comparatively small fields trigger 4p in the whole range of  $\mathcal{J}_L$ . In the 1D case, the FM couplings provide us with a similar progressive increment in the plateau’s magnetization as the magnetic field increases, with quenching of the magnetization at zero fields for a mixture of  $S_{(1,i),(2,j)}$  spins in the  $\mathcal{J}_A$  case; the AFM couplings, on the other hand, provide us with quenching of the magnetization at zero/low field for intermolecular couplings that do not mix spins  $S_{(1,i),(2,j)}$ . For all the configurations of 1D, comparatively small/intermediate fields trigger 2p and 4p in the whole range of  $\mathcal{J}$ .

By comparing the zones in the magnetization phase diagrams where the plateaus occur, with the entanglement entropy diagrams in Figure A4 (taken at the intermolecular bonds  $\mathcal{J}_{L,A,P}$ ), we see equivalent “#p” related to different entanglements between the individual SMMs at each configuration. The involvement of the central spins  $S_{(2,i)}$  favors the increase in the magnetization while decreasing the entanglement between the two SMMs at several magnetic fields; this partially occurs because the  $S_{(2,i)}$  in the nn SMM could be used to dimerize [41] and/or factorize the Hilbert space [31,41], for particular cases of the exchange couplings in the same way that, for the single molecule, the total  $S_z$  for spins  $S_{(1,i),(3,i)}$  together with the total  $S$  for the whole trimer can be used to resolve the gs [41].

Nonetheless, in the next section, we will see that such magnetization/entanglement behavior seems to be more fruitful if the SMM exchange is quenched close to the 1D

case. For  $\mathcal{J}_{A,P}$ , all in all, less entanglement for larger magnetization means setting FM intermolecular couplings for the 3D SMM with  $\mathcal{J}_A$  (or a weak AFM if larger fields), whereas the 1D SMM would favor the AFM coupling with  $\mathcal{J}_P$  (or a weak FM if larger fields). Hence, Figures 7 and A4 suggest exploring small  $\mathcal{J}$  values within a range where the interaction is large enough to capture most of the interesting physics of the FM/AFM interaction between two nn molecules but low enough compared to the initial 3D couplings ( $J$  six times and  $J_{13}$  four times larger), which are the ones corresponding to larger SWCNT diameters prior to quenching while being sufficient for the width of the 1D SMM magnetization plateaus so as not to change with small variations of such an interaction. This should allow us to obtain valuable insights into the physics of larger spin chains. According to this and for the sake of simplicity, we consider the two values  $\mathcal{J} = \pm 0.25$  as plausible intermolecular couplings and employ them in the calculation of finite-length molecular chains described in the following section, where we will change the intermolecular/intramolecular coupling ratio by applying 3D-to-1D SMM quenching.

#### 4. Chain Magnets

In what follows, we study coupled SMMs from a many-body perspective while artificially mimicking the confinement by quenching the intramolecular couplings from the 3D molecules into 1D. We use two intermolecular coupling strengths (FM and AFM for each configuration) as described in Section 3. There is no known adiabatic path to tune the exchange interactions while the molecules are being confined through the shrinking of the SWCNT diameters; hence, we propose a linear modulation of the ( $J, J_{13}$ ) interactions through changes in ( $x, y$ ) as modeled in Section 2.

##### 4.1. Beyond Two SMMs

In Figure 8, the magnetization along the field for spin chains with different numbers of SMMs is presented. We shall identify several molecules  $N_m$  that allow us to analyze the changes in local spins along the chains, whereas it is large enough to represent what occurs in large chains. For this analysis, in Figure 8,  $J$  and  $J_{13}$  correspond to the 3D SMM. As the insets in the figure show, for chains with  $N_m = 6$  (18 spins,  $S = 1$ ), the magnetization plateaus and the field-driving of the magnetization are already well-scaled. Below this number of molecules, the chains are more sensitive to low/intermediate fields for AFM couplings and the boundary conditions, especially for  $\mathcal{J}_{A,P}$ .

We focus on the wider plateaus because they are more stable when considering the temperature effects illustrated in Figure 6. These plateaus are also well converged when identified in the bipartite entanglement, as we can see in Figure 9, where the chains are partitioned between two nn molecules. We will enumerate the molecules/spins from left to right when convenient and without loss of generality while recalling the (1, 2, 3) convention shown in Figure 2 for each SMM. Thence, if we move from one intermolecular partition, i.e., spin 3(1) in one molecule to spin 1(3) in the nn molecule left-to-right (right-to-left), to another and toward the center of the chains, the fields defining the width of the plateaus are just slightly more defined from  $N_m \geq 6$ .

In Figure 9, the only difference between a different  $N_m$  at a particular configuration is given for AFM  $\mathcal{J}_P$ , which is due to odd  $N_m$  numbers, as for those, there are unpaired  $S_{(2,i)}$  at the borders that are not forming nn dimers (between adjacent molecules) and give rise to small low-field plateaus as they are easy to align; the FM case does not present this behavior, as spins-2 are already aligned with the  $J$ -dominated  $S_{(2,j)}$  sublattice as the magnetization suggests when comparing AFM and FM cases. Such FM cases are more interesting when the entanglement is evaluated by partitioning the chain within a particular molecule, as we can see in Figure A5, where the entanglement is evaluated at a partition between spins  $S_{(1,i)}$  and  $S_{(2,i)}$  of molecule three (spins seven and eight along the chain).

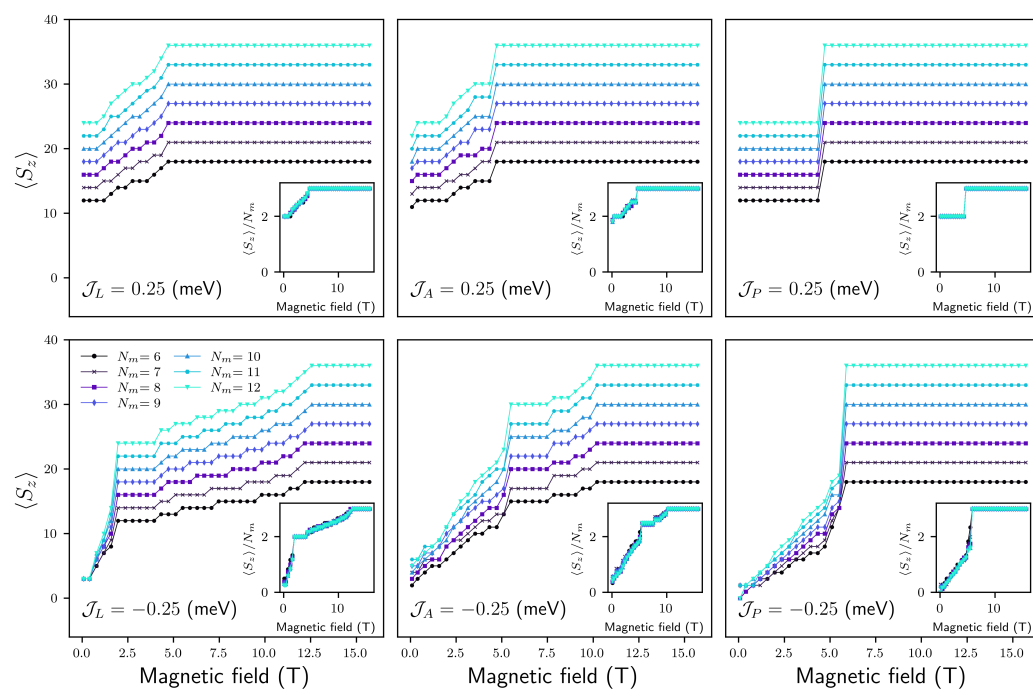


**Figure 8.** Magnetization along the field for  $\mathcal{J}_{L,A,P} = (0.25, -0.25)$  (top panels and bottom panels, respectively) for a different number of coupled SMMs. Inset: scaled magnetization.

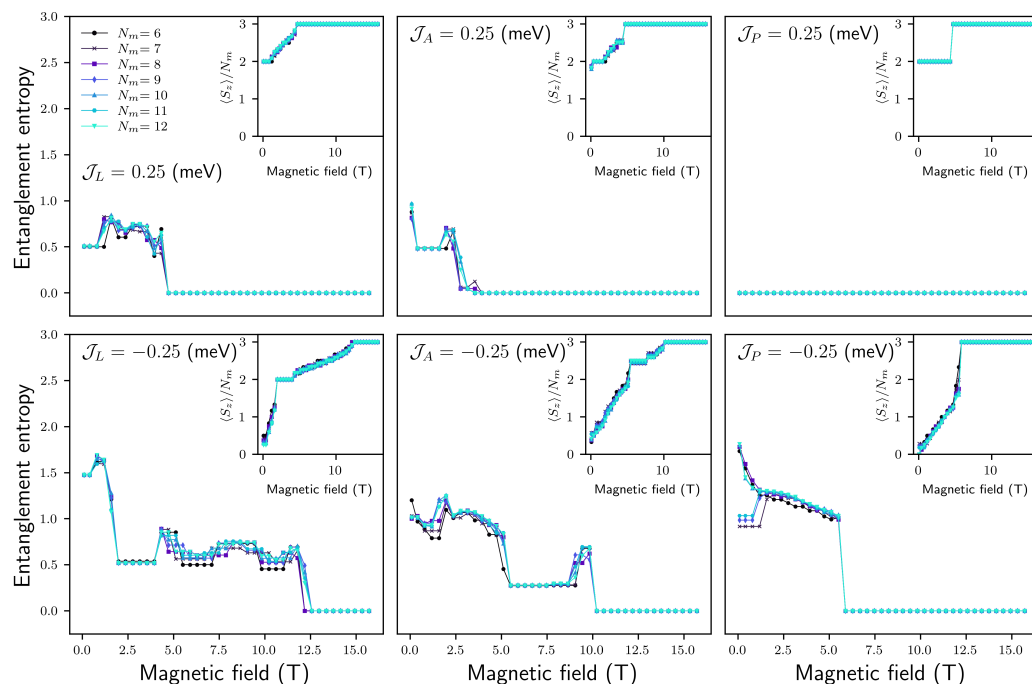


**Figure 9.** Entanglement entropy for the corresponding panels in Figure 8. The partitions of the chains are made by cutting between molecules 3 and 4 in each case (left-to-right).

Figures 9 and A5 show plateaus at the same field regions but with a staggered behavior when compared to each other. In order to understand this difference, in Figure 10, we present the results of the chains purposely partitioned between several nn intramolecular spins pairs for different  $N_m$ ; partitions between two nn SMMs yield slightly different results for these lengths, as already mentioned above. In this last figure, we can observe such staggered behavior for distinct odd and even chain lengths.  $\mathcal{J}_{L,P}$  do not present differences; however,  $\mathcal{J}_A$  displays two groups of chains that yield two different plateaus in at least one region of field, i.e.,  $N_m = (6, 10, 11)$  and  $N_m = (7, 8, 9, 12)$ . What those

chains have in common when tracking their partition points (caption in Figure 10) is that the first group is cutting the chain in different points between spins  $S_{(1,i)}$  and  $S_{(2,i)}$  of a molecule with a “perpendicular-like” ( $S_{(2,j)}$  in the intermolecular coupling) topology. In contrast, the second group is cutting them between  $S_{(1,i)}$  and  $S_{(2,i)}$  of a molecule with a “linear-like” ( $S_{(1,i)}$  or  $S_{(3,i)}$  in the intermolecular coupling) topology. Analyzing that further, we recognize that  $\mathcal{J}_{L,P}$  each have a period (with respect to moving in between pairs of nn sites along the chains) for the coupling topology that is half of that of  $\mathcal{J}_A$ , i.e., the aforementioned “perpendicular” partition for  $N_m = (6, 10, 11)$  is performed between a  $S_{(1,i)}$  with two local couplings and a  $S_{(2,i)}$  with two local couplings plus an intermolecular one or ( $S_{(1,i)}^2, S_{(2,i)}^3$ ) (the other way around for “linear” ( $S_{(1,i)}^3, S_{(2,i)}^2$ )), which will be repeated along the chain six intersites later (before) (three for ( $S_{(1,i)}^2, S_{(2,i)}^3$ ) in  $\mathcal{J}_P$  and ( $S_{(1,i)}^3, S_{(2,i)}^2$ ) in  $\mathcal{J}_L$ ).

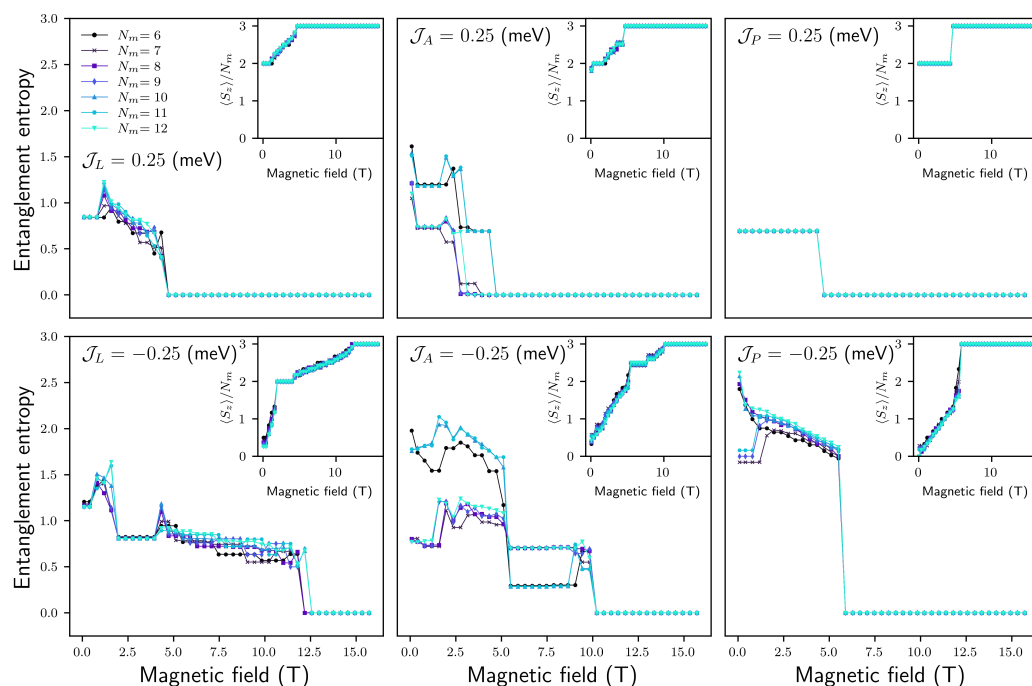


**Figure 10.** Entanglement entropy for the corresponding panels in Figure 8. The partitions of the chains are purposely made such that for even  $N_m$ , the cut is between spins 1 and 2 of the first molecule of the right chain with respect to the middle intermolecular point; we call it half-bond+1. For odd  $N_m$ , the middle molecules 4, 5, and 6 are included in the left chain for 7 and in the right chain for 9 and 11, respectively, with the half-bond+1 taken at that first molecule of the right chain similarly.

The entanglement in Figures 9 and A5 reflect two different types of exchange interaction topologies given by the way two nn SMMs are coupled. An implication of this is that it is likely that the way we confine the SMMs into the SWCNTs could be detected (among our three configurations), i.e., the resulting configuration could be distinguished if we happen to have thermal observables that witness the entanglement properties [3,9,10] along with the plateaus on the magnetization.

The strength of the non-saturated entanglement plateaus for  $\mathcal{J}_{L,P}$  depends on whether the partition is made at an intermolecular or intramolecular spin pair; meanwhile, for  $\mathcal{J}_A$ , it depends also on the type of intramolecular spin pairs. The relation of such plateaus with specific magnetization plateaus is more difficult to analyze from the above figures, as it compares local sites along chains with the translation symmetry breaking within two nn SMMs. Therefore, to obtain further insight in this regard, we will analyze the local sites while the intermolecular coupling is being quenched in the next section.

## 4.2. ( $J, J_{13}$ ) Quenching

In Figures 11–13, we present the entanglement entropy and corresponding local magnetization for  $\mathcal{J}_{L,A,P}$ , respectively. The intramolecular couplings are being quenched from top to bottom of such panels, as described above. In order to simplify the analysis for the number of sites to be displayed, we use  $N_m = 6$  in those figures (18 sites). Nevertheless, the results described here apply to  $N_m > 6$  as well, as illustrated in Figure A6. We will describe the features of spins at the end of the chains for completeness. However, the main characteristics reproducible in larger chains occur within the second and second-to-last intramolecular spin pairs.

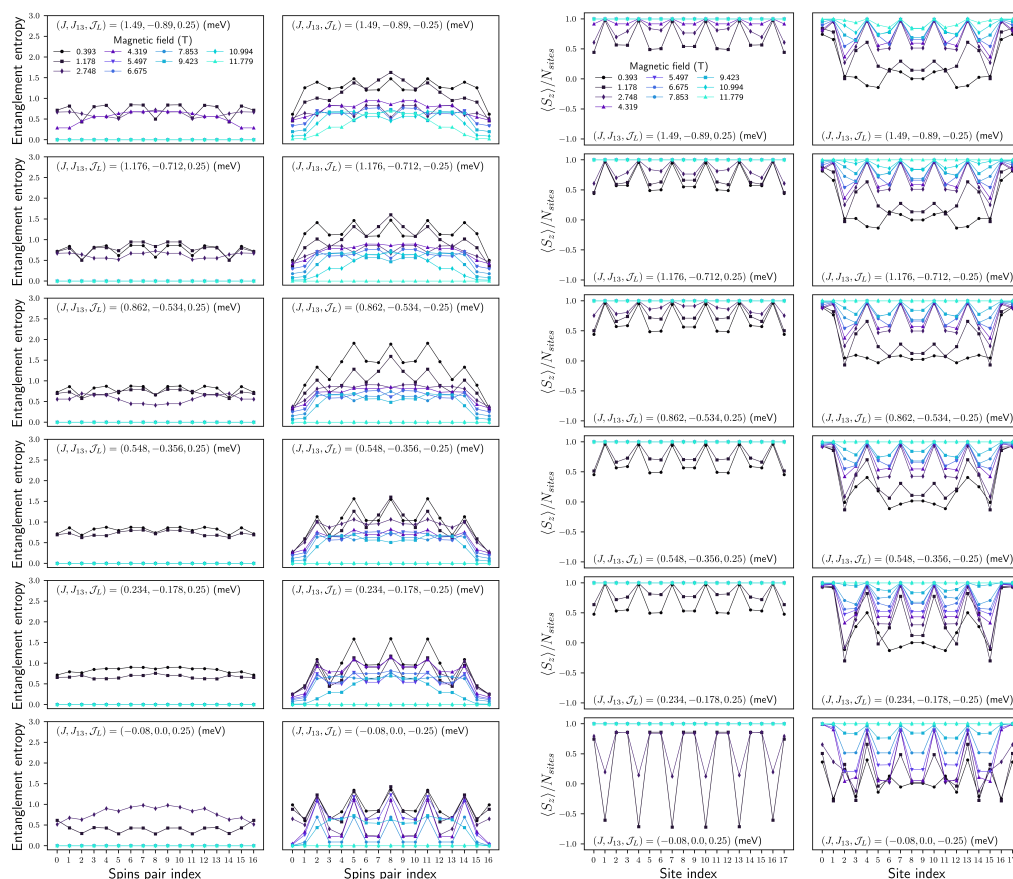


**Figure 11.** Entanglement entropy between each pair of molecular spins along the SWCNTs (columns 1 and 2, left-to-right) for  $\mathcal{J}_L = (0.25, -0.25)$ , selected magnetic fields, and  $(J, J_{13})$  being tuned from the 3D to 1D SMMs. Local magnetic moments at each molecular spin center along the spin chains inside the SWCNTs (columns 3, 4).

### 4.2.1. $\mathcal{J}_L$ Configuration

#### FM $\mathcal{J}_L$

Starting with ferromagnetically coupled 3D molecules in a linear arrangement ( $\mathcal{J}_L$ ), as depicted in Figure 11, the chain is organized FM, with spins  $S_{(2,j)}$  polarized at 1, and  $S_{(1,j)}$  and  $S_{(3,j)}$  simultaneously polarized between 0.5 and 1 depending on the field value (the larger the field, the closer to 1), forming effective dimers. This can be understood from the exact eigenstate of a single molecule (see Figure 6a), where the central spin can be factorized from the entangled  $S_{(1,j)}$ - $S_{(3,j)}$  pair. This picture, however, becomes distorted as intermolecular couplings are introduced, where significant correlations between adjacent molecules appear, as can be seen from their non-zero entanglement entropy.

As intramolecular couplings undergo quenching at specific field values, effective dimers between adjacent molecules also experience a decrease in spin as long as  $J$  is ferromagnetic. When  $J$  becomes AFM for 1D molecules, the chain maintains the ferromagnetic

arrangement between molecules as the intermolecular coupling dominates. At the same time, the spins within each molecular unit align antiparallel (with  $S_{(2,j)}$  taking negative fractional values), opposing the dimers. In scenarios of low values of  $J_{13}$ , where  $J$  and the intermolecular coupling compete, dimers facilitate entanglement tuning across chain sites at low fields. For 1D couplings, the magnetism of such dimers remains frozen at very low fields, with the total magnetization relaxed by AFM-polarized  $S_{(2,j)}$ . Modulating entanglement along the chains is feasible at low fields, but it quenches for moderate and large fields.

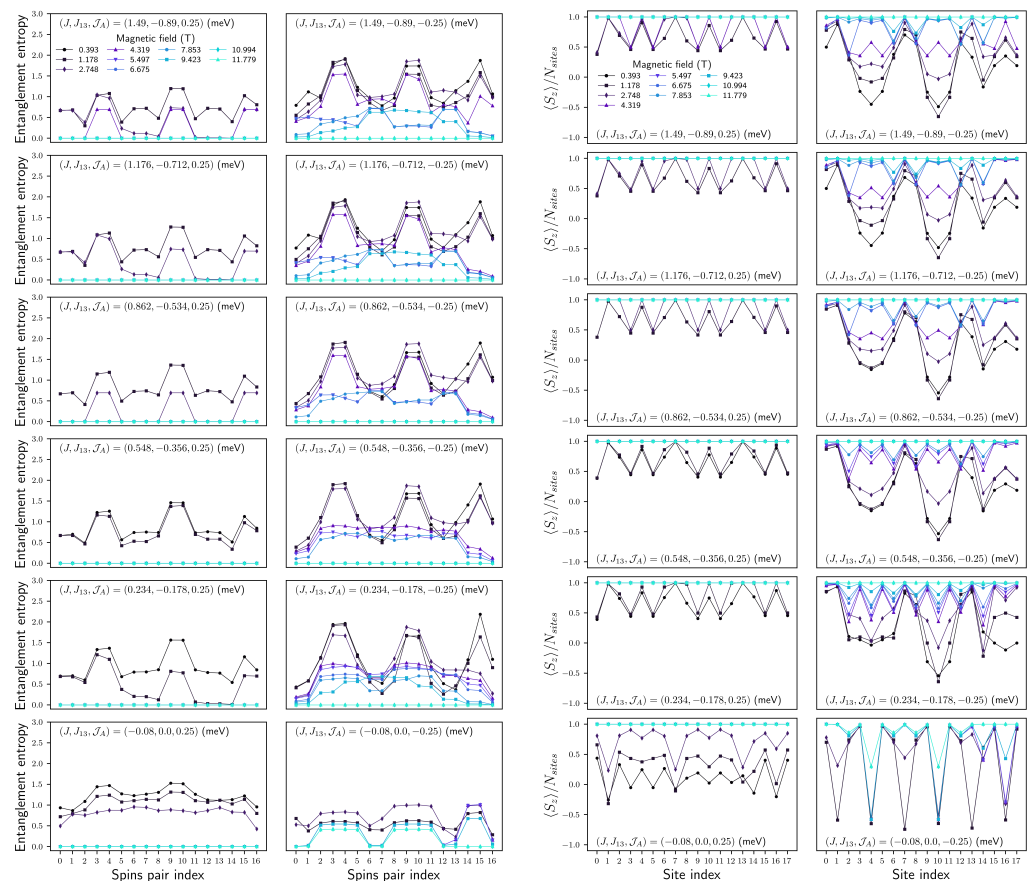


**Figure 12.** Entanglement entropy between each pair of molecular spins along the SWCNTs (columns 1 and 2, left-to-right) for  $\mathcal{J}_A = (0.25, -0.25)$ , selected magnetic fields, and  $(J, J_{13})$  being tuned from the 3D to 1D SMMs. Local magnetic moments at each molecular spin center along the spin chains inside the SWCNTs (columns 3, 4).

### AFM $\mathcal{J}_L$

The AFM intermolecular coupling has a similar behavior to the FM case, with dimers formed by  $S_{(1,i)}$  and  $S_{(3,j)}$  in neighboring molecules. Intermediate and large fields maintain these dimers, with small fields decreasing the magnetization until they are destroyed. This dimeric behavior dominates the first plateau in the magnetization landscape. The quenching effect accelerates the demagnetization of the dimers, taking the FM to an AFM system from 3D to 1D, respectively. AFM intermolecular coupling always competes with  $J_{13}$ , and for 1D, with the latter nullified, the chain ends are demagnetized unless the field is high. The entanglement at these points is minimized during quenching, but when  $J_{13}$  is turned off, it releases the chain to become AFM at low fields, dominating the intermolecular entanglement.

The quenching allows lower fields to modulate the magnetization of the dimers, but the polarization of edge sites is lost as  $J_{13}$  approaches zero. Throughout quenching from 3D to 1D, the entanglement is very similar for intermediate and high fields, forming dimeric

plateaus given by the points between intramolecular spins that dominate the landscape. The latter shows maxima for intermolecular bonds (in the  $\mathcal{J}_L$  case; there is always a bond between  $S_{(1,i)}$  and  $S_{(3,j)}$ ) at low fields. This is more evident for 1D, where the intramolecular entanglement decreases faster for intermediate and high fields.

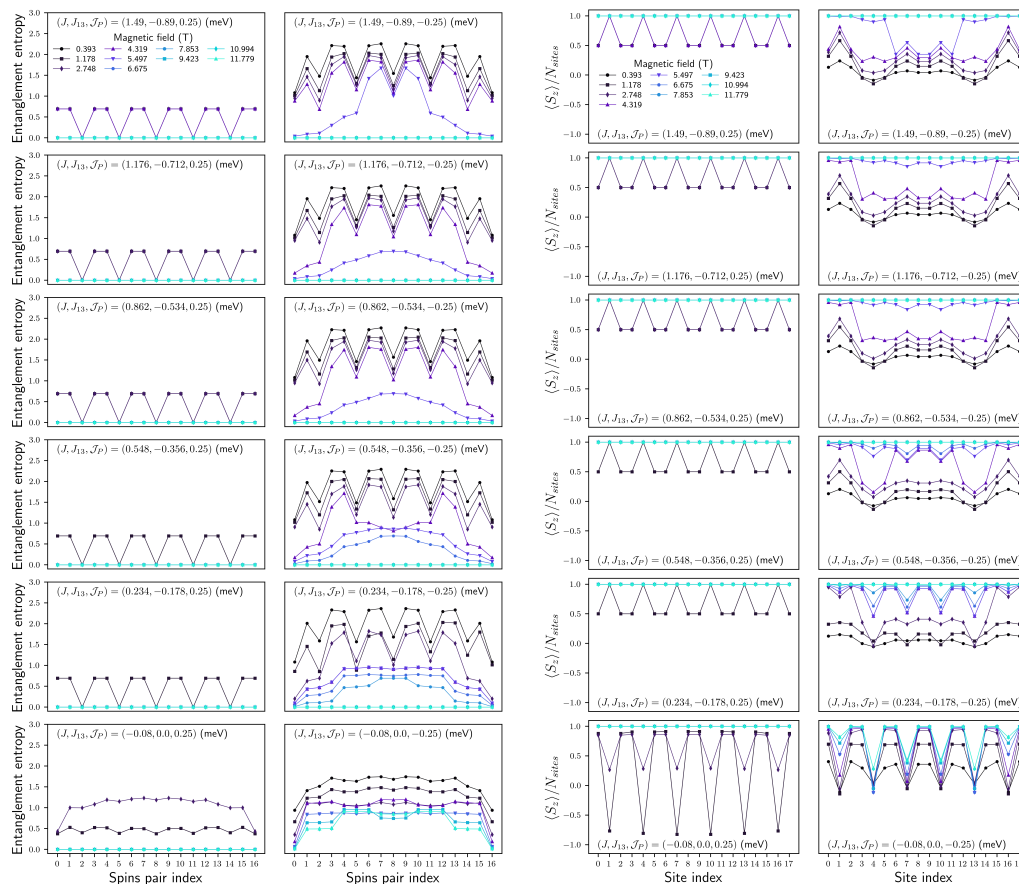


**Figure 13.** Entanglement entropy between each pair of molecular spins along the SWCNTs (columns 1 and 2, left-to-right) for  $\mathcal{J}_p = (0.25, -0.25)$ , selected magnetic fields, and  $(J, J_{13})$  being tuned from the 3D to 1D SMMs. Local magnetic moments at each molecular spin center along the spin chains inside the SWCNTs (columns 3, 4).

#### 4.2.2. $\mathcal{J}_A$ Configuration

##### FM $\mathcal{J}_A$

The quenching does not significantly affect the FM-coupled chain with the alternated configuration, as it maintains FM order unless  $J_{13}$  is zero for 1D. At very small fields,  $S_{(1,i)}$  and  $S_{(3,j)}$  oscillate between 0.5 and 1.0 in a staggered manner while  $S_{(2,j)}$  are polarized. The quenching breaks the polarization for the  $S_{(2,i)}$  in the locally “perpendicular-like” molecules for very small fields. In 1D, the previous behavior is inverted as in the linear case, with a larger magnetization for  $S_{(1,i)}$  and  $S_{(3,j)}$  being able to generate an AFM system at low fields due mainly to the inversion of  $S_{(2,j)}$ . The entanglement also has a valley-type behavior, showing small plateaus formed by intramolecular spin pairs, in this case asymmetrically, with spin pairs within locally “linear-like” molecules showing less entanglement and spin pairs coupling neighboring molecules being even less entangled. This behavior is notable at low fields, though it disappears with quenching. In 1D, it is possible to find small fields that generate entanglement plateaus along the chains, with a behavior similar to FM-coupled linear chains. In contrast, the dominant behavior of 3D molecules is not observed at intermediate/high fields. At intermediate and high fields, the system is easily polarized.

### AFM $\mathcal{J}_A$

The alternated chain with AFM coupling has a similar behavior with the quenching for 3D-like spins, in which locally “linear-like” molecules are closer to being polarized than locally “perpendicular-like” molecules, generating a valley-like magnetization. The system is AFM for low fields and FM for intermediate and high fields, making it possible to polarize with lower fields from 3D to 1D. For intermediate fields and close to 1D, we have a zigzag-type magnetization with the polarization of the spins, starting from a locally “perpendicular” molecule, such that intramolecular  $S_{(1,i)}$  and  $S_{(3,i)}$  are polarized for certain intermediate and large fields, regardless of the local molecule, and quenched or negative for small field values.  $S_{(2,i)}$  are less polarized as the field goes down.

Therefore, the entanglement has two main zones depending on the field, one for a low field with a staggered behavior similar to the FM case, while for intermediate and high fields, plateaus are formed, which are then divided into two 1D plateaus for each set of three molecules, i.e., “(linear–perpendicular–linear)-like”; a magnetization minimum is located between two valleys. The 1D accentuates the previous behavior, and it is possible to have clear plateaus formed by such sets of three molecules for a specific field range. The magnetization corresponding to these plateaus can be FM for high fields, and for low fields, the system can be AFM, again with  $S_{(2,i)}$  opposing  $S_{(1,i)}$  and  $S_{(3,i)}$ . In these entanglement plateaus, the polarization in the “perpendicular-like”  $S_{(2,i)}$  can be changed within a field range without changing the entanglement while topologically protecting them with the linear molecules.

#### 4.2.3. $\mathcal{J}_P$ Configuration

##### FM $\mathcal{J}_P$

In the case of intermolecular FM exchange in a perpendicular chain, the quenching from 3D has no effect. The system is dimerized to tiny fields, with intramolecular  $S_{(1,i)}$  and  $S_{(3,i)}$  at 0.5 while  $S_{(2,i)}$  are polarized. The change to 1D reverses the behavior as in previous cases, dominating the intermolecular coupling. A locally AFM system can be generated at a low field with  $S_{(1,i)}$  and  $S_{(3,j)}$  dimerized, and  $S_{(2,i)}$  can change polarization with the field. The entanglement also has a staggered behavior, showing a quenching between  $S_{(1,i)}$  and  $S_{(3,j)}$  for a wide field range, except at very small ones. When moving to 1D-like chains, the system shows entanglement at low fields without a clear staggered behavior. It is also possible to find fields for which the entanglement is similar between all spin pairs along the chain.

##### AFM $\mathcal{J}_P$

In the perpendicular AFM chain, the magnetization partially imitates the  $\mathcal{J}_A$  configuration with respect to the local “perpendicular-like” molecules, and we have a zigzag-type behavior for low fields for which the FM magnetization oscillates from site to site. In this case, the system is more sensitive to the boundaries, and there seem to be two magnetization valleys; however, this configuration has local inversion symmetry, and the magnetization can only change due to the different coupling topologies of nn molecules.

The quenching causes non-polarized systems with slightly oscillating magnetization between  $S_{(2,i)}$  and  $S_{(1,i)}$ - $S_{(3,j)}$  to become polarized in a dimeric manner, with  $S_{(1,i)}$ - $S_{(3,j)}$  polarized with a higher magnetization. There is a range of intermediate fields in which only the  $S_{(2,i)}$  magnetization changes with the field, where intermolecular couplings are close to 1D. Near 1D, it is also possible to find fields for which the magnetization at each site along the chain is approximately similar and close to zero. In 1D, we have a marked dimeric magnetization given by the  $S_{(1,i)}$ - $S_{(3,j)}$  pair that remains polarized over a wide field range, with  $S_{(2,i)}$  being modulated with the field between positive and negative values.

On the other hand, the entanglement has a staggered behavior with minima between spin pairs of neighboring molecules. The entanglement decreases for a specific field and as the system goes from 3D to 1D. As we reach 1D, the entanglement forms plateaus from intermediate fields, with a staggered behavior at high fields similar to  $\mathcal{J}_A$  but for finite entanglements. For intermediate fields, it is possible to find field values for which the entanglement is uniform throughout the entire chain.

Summarizing this section, the investigation into various configurations reveals intriguing possibilities for the magnetic ordering of molecular chains.

The linear configuration shows dominance of magnetization by dimers formed by nearest-neighbor spins of adjacent molecules. Spins can be tuned when close to 3D coupling or locally protected in the 1D limit. The entanglement across the chain can be tuned to be nearly uniform for FM coupling between the molecules. This configuration could represent smaller nanotube diameters for encapsulation.

Alternated chains effectively divide into trimers with a zigzag magnetization and are susceptible to switching between FM/AFM (3D) for small fields. For 1D molecules, a factorization of the central spins of such trimeric structures is possible at large fields. This behavior, also characterized by entanglement plateaus, suggests an effective protection of these trimers. From a structural viewpoint, this configuration would be the least stable.

In the perpendicular arrangement, a similar behavior to linear FM is possible when intermolecular exchange is also FM, but with dimers formed within the molecule, while the AFM case resembles an alternated chain. In the 1D limit, frozen intermolecular dimers are found along tunable central spins, with a single entanglement plateau across the chain. This configuration would be possible for larger diameters of the SWCNTs.

## 5. Conclusions

In this work, we have studied the magnetic and entanglement properties of one-dimensional confined trimetric nickel(II) molecules using Exact Diagonalization and Matrix Product States. We modeled the confinement of such molecules by mimicking the change in the experimentally obtained intramolecular exchange interactions for different SWCNT diameters with linear quenching. We also introduced intermolecular couplings considering three different interaction topologies.

Using two representative intermolecular couplings, we performed many-body calculations. We found distinct signatures of the interaction topology of the molecules inside the SWCNTs, reflected in the magnetism of the encapsulated molecular units.

We showed that the  $\mathcal{J}_L$  coupling offers tunability for 3D molecules and protects magnetization in the 1D case, enabling FM/AFM switching. An effective protection with FM/AFM switchability in a trimer structure is found in the alternated configuration. The parallel configuration with FM  $\mathcal{J}_P$  behaves as a disentangled dimer structure but resembles  $\mathcal{J}_A$  in AFM, presenting protection for 1D-like molecules.

Finally, these insights could provide versatile control strategies for molecular chains and valuable information about the interplay between topology and confinement, particularly in encapsulated molecular magnets in single-walled carbon nanotubes.

**Author Contributions:** Conceptualization, J.M.F. and J.I.N.L.; methodology, J.M.F. and E.A.C.E.; software, J.I.N.L., E.A.C.E. and J.M.F.; validation, J.I.N.L., E.A.C.E., E.S.M. and J.M.F.; formal analysis, J.I.N.L., E.A.C.E., E.S.M. and J.M.F.; investigation, J.I.N.L., E.A.C.E., E.S.M. and J.M.F.; resources, E.S.M. and J.M.F.; data curation, J.I.N.L., E.A.C.E. and J.M.F.; writing—original draft preparation, J.I.N.L., E.A.C.E., E.S.M. and J.M.F.; writing—review and editing, J.I.N.L., E.A.C.E., E.S.M. and J.M.F.; visualization, J.I.N.L. and E.A.C.E.; supervision, J.M.F.; project administration, E.A.C.E. and J.M.F.; funding acquisition, E.A.C.E. and J.M.F. All authors have read and agreed to the published version of this manuscript.

**Funding:** E.A.C.E., E.S.M. and J.M.F. acknowledge financial support from FONDECYT Regular 1221301 (Chile) and USM-DGIIIE Proyecto Investigación PI-LII-23-09.

**Institutional Review Board Statement:** Not applicable.

**Informed Consent Statement:** Not applicable.

**Data Availability Statement:** Details of MPS simulations are available upon reasonable request to [juanmanuel.florez@usm.cl](mailto:juanmanuel.florez@usm.cl).

**Conflicts of Interest:** The authors declare no conflict of interest.

## Abbreviations

The following abbreviations are used in this manuscript:

Ni(acac) <sub>2</sub>	trimeric nickel(II) acetylacetonate
SMM	single-molecule magnet
nn	nearest-neighbor
<i>L</i>	linear
<i>A</i>	alternated
<i>P</i>	perpendicular
SWCNT	single-wall carbon nanotube
MPSs	Matrix Product States
DMRG	density-matrix renormalization group
Tenpy	Tensor Network Python
TDVPs	time-dependent variational principles
TEBDs	time-evolving block decimations
<i>S</i>	entanglement entropy or von Neumann's
FM	ferromagnetism
AFM	antiferromagnetism

## Appendix A. Exact Solution for One and Two SMM

**Table A1.** Energies (left) corresponding to the eigenstates (right) of the 3D Ni(acac)<sub>2</sub> levels.

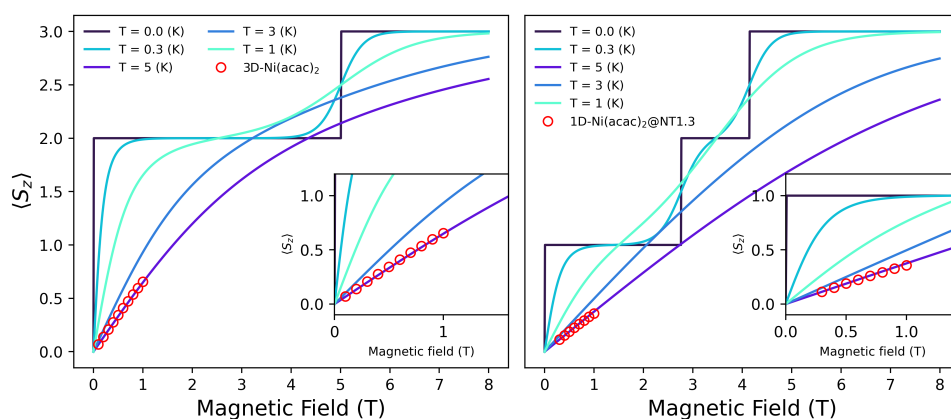
Energy (meV)	State
−4.76	$\frac{1}{\sqrt{2}}( \downarrow\downarrow 0\rangle -  0\downarrow\downarrow\rangle)$
−4.76	$\frac{1}{2}( \downarrow 00\rangle +  \downarrow\downarrow\uparrow\rangle -  00\downarrow\rangle -  \uparrow\downarrow\downarrow\rangle)$
−4.76	$\frac{1}{2\sqrt{3}}( 0\downarrow\uparrow\rangle -  0\uparrow\downarrow\rangle + 2 \downarrow 0\downarrow\rangle +  \downarrow\uparrow 0\rangle - 2 \uparrow 0\downarrow\rangle -  \uparrow\downarrow 0\rangle)$
−4.76	$\frac{1}{2}( 00\uparrow\rangle +  \downarrow\uparrow\uparrow\rangle -  \uparrow 00\rangle -  \uparrow\uparrow\downarrow\rangle)$
−4.76	$\frac{1}{\sqrt{2}}( 0\uparrow\uparrow\rangle -  \uparrow\uparrow 0\rangle)$
−4.18	$\frac{1}{\sqrt{3}}( 0\downarrow\downarrow\rangle +  \downarrow 0\downarrow\rangle +  \downarrow\downarrow 0\rangle)$
−4.18	$\frac{1}{\sqrt{15}}(2 00\downarrow\rangle + 2 0\downarrow 0\rangle + 2 \downarrow 00\rangle +  \downarrow\downarrow\uparrow\rangle +  \downarrow\uparrow\downarrow\rangle +  \uparrow\downarrow\downarrow\rangle)$
−4.18	$\frac{1}{\sqrt{10}}(2 000\rangle +  0\downarrow\uparrow\rangle +  0\uparrow\downarrow\rangle +  \downarrow 0\uparrow\rangle +  \uparrow\downarrow 0\rangle +  \uparrow 0\downarrow\rangle +  \uparrow\downarrow 0\rangle)$
−4.18	$\frac{1}{\sqrt{15}}(2 00\uparrow\rangle + 2 0\uparrow 0\rangle + 2 \uparrow 00\rangle +  \downarrow\uparrow\uparrow\rangle +  \uparrow\downarrow\uparrow\rangle +  \uparrow\uparrow\downarrow\rangle)$
−4.18	$\frac{1}{\sqrt{3}}( 0\uparrow\uparrow\rangle +  \uparrow 0\uparrow\rangle +  \uparrow\uparrow 0\rangle)$
−4.18	$ \uparrow\uparrow\uparrow\rangle$
−3.56	$\frac{1}{\sqrt{3}}(- 0\downarrow 0\rangle +  \downarrow\downarrow\uparrow\rangle +  \uparrow\downarrow\downarrow\rangle)$
−3.56	$\frac{1}{\sqrt{3}}(- 000\rangle +  \downarrow 0\uparrow\rangle +  \uparrow 0\downarrow\rangle)$
−3.56	$\frac{1}{\sqrt{3}}(- 0\uparrow 0\rangle +  \downarrow\uparrow\uparrow\rangle +  \uparrow\uparrow\downarrow\rangle)$
1.2	$\frac{1}{2}( 00\downarrow\rangle -  \downarrow 00\rangle +  \downarrow\downarrow\uparrow\rangle -  \uparrow\downarrow\downarrow\rangle)$
1.2	$\frac{1}{2}(- 0\downarrow\uparrow\rangle -  0\uparrow\downarrow\rangle +  \downarrow\uparrow 0\rangle +  \uparrow\downarrow 0\rangle)$
1.2	$\frac{1}{2}(- 00\uparrow\rangle +  \downarrow\uparrow\uparrow\rangle +  \uparrow 00\rangle -  \uparrow\uparrow\downarrow\rangle)$
4.18	$\frac{1}{\sqrt{6}}(- 0\downarrow\uparrow\rangle +  0\uparrow\downarrow\rangle +  \downarrow 0\uparrow\rangle -  \downarrow\uparrow 0\rangle -  \uparrow 0\downarrow\rangle +  \uparrow\downarrow 0\rangle)$
4.76	$\frac{1}{\sqrt{6}}( 0\downarrow\downarrow\rangle - 2 \downarrow 0\downarrow\rangle +  \downarrow\downarrow 0\rangle)$
4.76	$\frac{1}{2\sqrt{3}}(- 00\downarrow\rangle + 2 0\downarrow 0\rangle -  \downarrow 00\rangle +  \downarrow\downarrow\uparrow\rangle - 2 \downarrow\uparrow\downarrow\rangle +  \uparrow\downarrow\downarrow\rangle)$
4.76	$\frac{1}{2}(- 0\downarrow\uparrow\rangle +  0\uparrow\downarrow\rangle +  \downarrow\uparrow 0\rangle -  \uparrow\downarrow 0\rangle)$
4.76	$\frac{1}{2\sqrt{3}}(- 00\uparrow\rangle + 2 0\uparrow 0\rangle +  \downarrow\uparrow\uparrow\rangle -  \uparrow 00\rangle - 2 \uparrow\downarrow\uparrow\rangle +  \uparrow\uparrow\downarrow\rangle)$

Table A1. Cont.

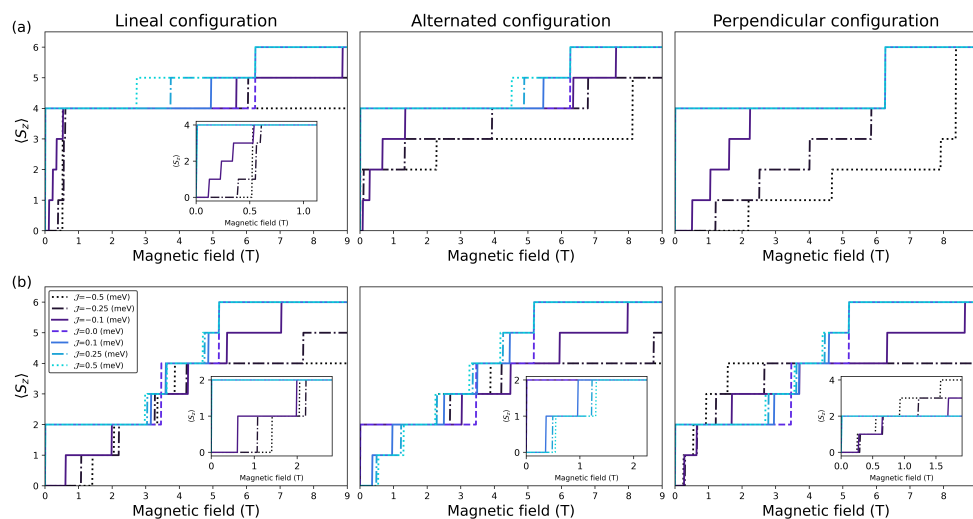
Energy (meV)	State
4.76	$\frac{1}{\sqrt{6}}( 0 \uparrow \uparrow\rangle - 2 \uparrow 0 \uparrow\rangle +  \uparrow \uparrow 0\rangle)$
10.72	$\frac{1}{2\sqrt{15}}(-3 00 \downarrow\rangle + 2 0 \downarrow 0\rangle - 3 \downarrow 00\rangle +  \downarrow \downarrow \uparrow\rangle + 6 \downarrow \downarrow \downarrow\rangle +  \uparrow \downarrow \downarrow\rangle)$
10.72	$\frac{1}{2\sqrt{15}}(4 000\rangle - 3 0 \downarrow \uparrow\rangle - 3 0 \uparrow \downarrow\rangle + 2 \downarrow 0 \uparrow\rangle - 3 \downarrow \uparrow 0\rangle + 2 \uparrow 0 \downarrow\rangle - 3 \uparrow \downarrow 0\rangle)$
10.72	$\frac{1}{2\sqrt{15}}(-3 00 \uparrow\rangle + 2 0 \uparrow 0\rangle +  \downarrow \uparrow \uparrow\rangle - 3 \uparrow 00\rangle + 6 \uparrow \downarrow \uparrow\rangle +  \uparrow \uparrow \downarrow\rangle)$

Table A2. Energies (left) corresponding to the eigenstates (right) of the 1D Ni(acac)<sub>2</sub> levels.

Energy (meV)	State
-0.48	$\frac{1}{2\sqrt{15}}(-3 00 \downarrow\rangle + 2 0 \downarrow 0\rangle - 3 \downarrow 00\rangle) +  \downarrow \downarrow \uparrow\rangle + 6 \uparrow \downarrow \uparrow\rangle +  \uparrow \downarrow \downarrow\rangle)$
-0.48	$\frac{1}{2\sqrt{15}}(4 000\rangle - 3 0 \downarrow \uparrow\rangle - 3 0 \uparrow \downarrow\rangle + 2 \downarrow 0 \uparrow\rangle - 3 \downarrow \uparrow 0\rangle + 2 \uparrow 0 \downarrow\rangle - 3 \uparrow \downarrow 0\rangle)$
-0.48	$\frac{1}{2\sqrt{15}}(-3 00 \uparrow\rangle + 2 0 \uparrow 0\rangle +  \downarrow \uparrow \uparrow\rangle - 3 \uparrow 00\rangle + 6 \uparrow \downarrow \uparrow\rangle +  \uparrow \uparrow \downarrow\rangle)$
-0.32	$\frac{1}{\sqrt{6}}(- 0 \downarrow \uparrow\rangle +  0 \uparrow \downarrow\rangle +  \downarrow 0 \uparrow\rangle -  \downarrow \uparrow 0\rangle -  \uparrow 0 \downarrow\rangle +  \uparrow \downarrow 0\rangle)$
-0.16	$\frac{1}{2}( 00 \downarrow\rangle -  \downarrow 00\rangle) +  \downarrow \downarrow \uparrow\rangle -  \uparrow \downarrow \downarrow\rangle)$
-0.16	$\frac{1}{2}(- 0 \downarrow \uparrow\rangle -  0 \uparrow \downarrow\rangle +  \downarrow \uparrow 0\rangle +  \uparrow \downarrow 0\rangle)$
-0.16	$\frac{1}{2}(- 00 \uparrow\rangle +  \downarrow \uparrow \uparrow\rangle +  \uparrow 00\rangle -  \uparrow \uparrow \downarrow\rangle)$
-0.16	$\frac{1}{\sqrt{6}}( 00 \downarrow\rangle - 2 \downarrow 0 \downarrow\rangle +  \downarrow \downarrow 0\rangle)$
-0.16	$\frac{1}{2\sqrt{3}}(- 00 \downarrow\rangle + 2 0 \downarrow 0\rangle -  \downarrow 00\rangle) +  \downarrow \downarrow \uparrow\rangle - 2 \downarrow \downarrow \downarrow\rangle +  \uparrow \downarrow \downarrow\rangle)$
-0.16	$\frac{1}{2}(- 0 \downarrow \uparrow\rangle +  0 \uparrow \downarrow\rangle +  \downarrow \uparrow 0\rangle -  \uparrow \downarrow 0\rangle)$
-0.16	$\frac{1}{2\sqrt{3}}(- 00 \uparrow\rangle + 2 0 \uparrow 0\rangle +  \downarrow \uparrow \uparrow\rangle -  \uparrow 00\rangle - 2 \uparrow \downarrow \uparrow\rangle +  \uparrow \uparrow \downarrow\rangle)$
-0.16	$\frac{1}{\sqrt{6}}( 0 \uparrow \uparrow\rangle - 2 \uparrow 0 \uparrow\rangle +  \uparrow \uparrow 0\rangle)$
0.0	$\frac{1}{\sqrt{3}}(- 0 \downarrow 0\rangle +  \downarrow \downarrow \uparrow\rangle +  \uparrow \downarrow \downarrow\rangle)$
0.0	$\frac{1}{\sqrt{3}}(- 000\rangle +  \downarrow 0 \uparrow\rangle +  \uparrow 0 \downarrow\rangle)$
0.0	$\frac{1}{\sqrt{3}}(- 0 \uparrow 0\rangle +  \downarrow \uparrow \uparrow\rangle +  \uparrow \uparrow \downarrow\rangle)$
0.16	$\frac{1}{\sqrt{2}}(- 0 \downarrow \downarrow\rangle +  \downarrow \downarrow 0\rangle)$
0.16	$\frac{1}{2}(- 00 \downarrow\rangle +  \downarrow 00\rangle) +  \downarrow \downarrow \uparrow\rangle -  \uparrow \downarrow \downarrow\rangle)$
0.16	$\frac{1}{2\sqrt{3}}( 0 \downarrow \uparrow\rangle -  0 \uparrow \downarrow\rangle + 2 \downarrow 0 \uparrow\rangle +  \downarrow \uparrow 0\rangle - 2 \uparrow 0 \downarrow\rangle -  \uparrow \downarrow 0\rangle)$
0.16	$\frac{1}{2}( 00 \uparrow\rangle +  \downarrow \uparrow \uparrow\rangle -  \uparrow 00\rangle -  \uparrow \uparrow \downarrow\rangle)$
0.16	$\frac{1}{\sqrt{2}}( 0 \uparrow \uparrow\rangle -  \uparrow \uparrow 0\rangle)$
0.32	$ \downarrow \downarrow \downarrow\rangle)$
0.32	$\frac{1}{\sqrt{3}}( 0 \downarrow \downarrow\rangle +  \downarrow 0 \downarrow\rangle +  \downarrow \downarrow 0\rangle)$
0.32	$\frac{1}{\sqrt{15}}(2 00 \downarrow\rangle + 2 0 \downarrow 0\rangle + 2 \downarrow 00\rangle) +  \downarrow \downarrow \uparrow\rangle +  \downarrow \downarrow \downarrow\rangle +  \uparrow \downarrow \downarrow\rangle)$
0.32	$\frac{1}{\sqrt{10}}(2 000\rangle +  0 \downarrow \uparrow\rangle +  0 \uparrow \downarrow\rangle +  \downarrow 0 \uparrow\rangle +  \downarrow \uparrow 0\rangle +  \uparrow 0 \downarrow\rangle +  \uparrow \downarrow 0\rangle)$
0.32	$\frac{1}{\sqrt{15}}(2 00 \uparrow\rangle + 2 0 \uparrow 0\rangle +  \downarrow \uparrow \uparrow\rangle + 2 \uparrow 00\rangle) +  \uparrow \downarrow \uparrow\rangle +  \uparrow \uparrow \downarrow\rangle)$
0.32	$\frac{1}{\sqrt{3}}( 0 \uparrow \uparrow\rangle +  \uparrow 0 \uparrow\rangle +  \uparrow \uparrow 0\rangle)$
0.32	$ \uparrow \uparrow \uparrow\rangle)$



**Figure A1.** Magnetization plateaus under different temperatures in 3D (left panel) and 1D (right panel) structures, compared to the experimental values (red circles) reported in [26].



**Figure A2.** Magnetization along the field for  $\mathcal{J}_L$ ,  $\mathcal{J}_A$ , and  $\mathcal{J}_P$  exchange-coupled pairs of molecules with (a) 3D molecular unit (upper panel) and (b) 1D molecular unit (lower panel) at 0.0 (K).

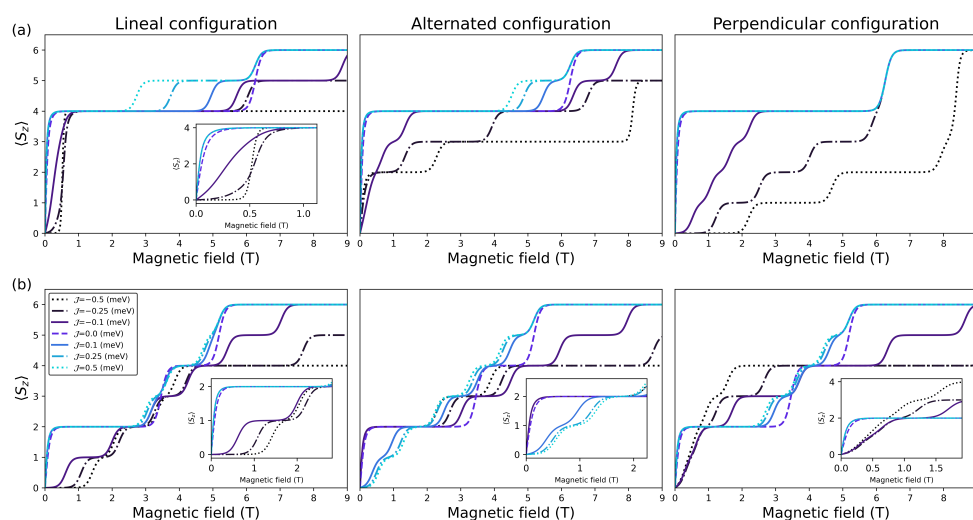


**Figure A3.** Magnetization along the field for  $\mathcal{J}_L$ ,  $\mathcal{J}_A$ , and  $\mathcal{J}_P$  exchange-coupled pairs of molecules with (a) 3D molecular unit (upper panel) and (b) 1D molecular unit (lower panel) at 0.1 (K).

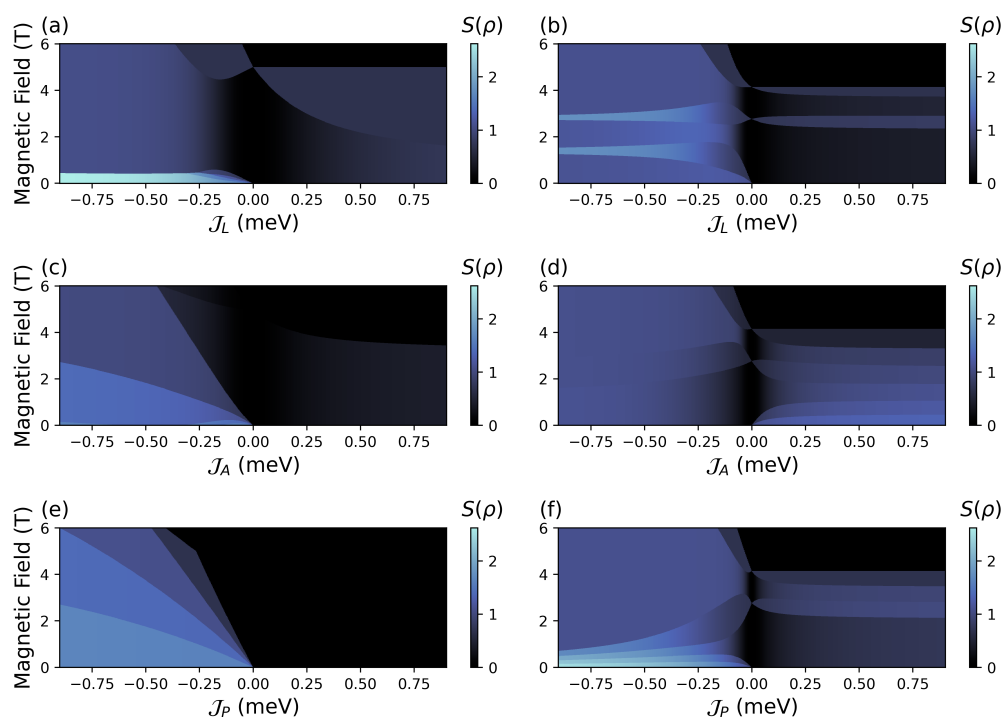


**Figure A4.** Entanglement entropy phase diagrams corresponding to  $\mathcal{J}_L$ ,  $\mathcal{J}_A$ , and  $\mathcal{J}_P$  configurations for the 3D molecules (a,c,e) (left column) and 1D ones (b,d,f) (right column), respectively.

## Appendix B. Entanglement of Chain Magnets

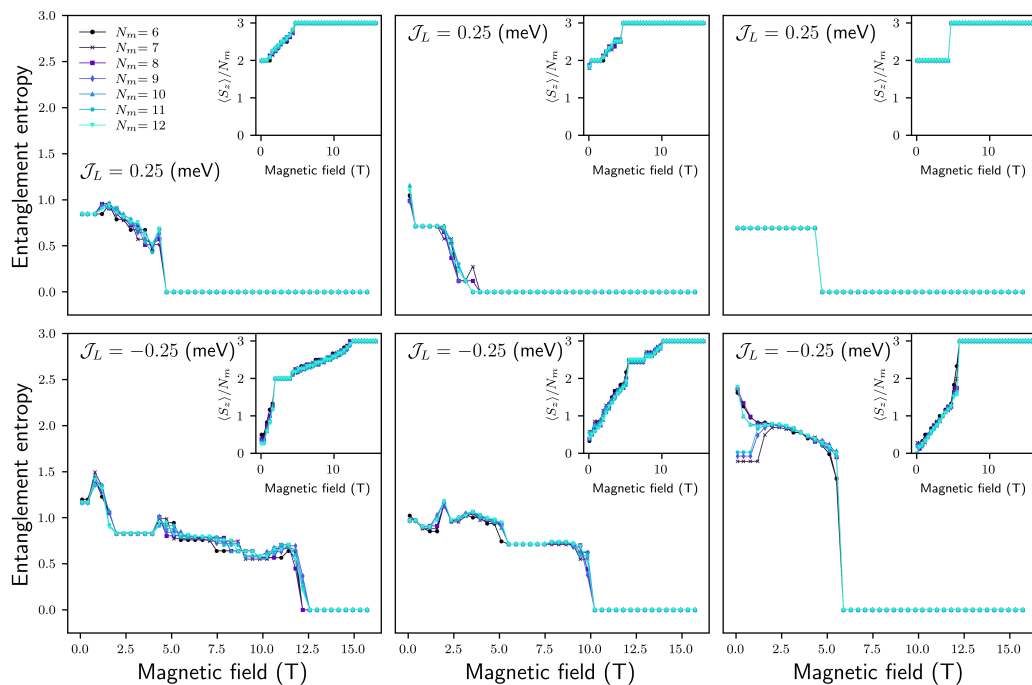


**Figure A5.** Entanglement entropy for the corresponding panels in Figure 8. The partitions of the chains are made by cutting them between spins 1 and 2 at molecule 3 for the corresponding cases.

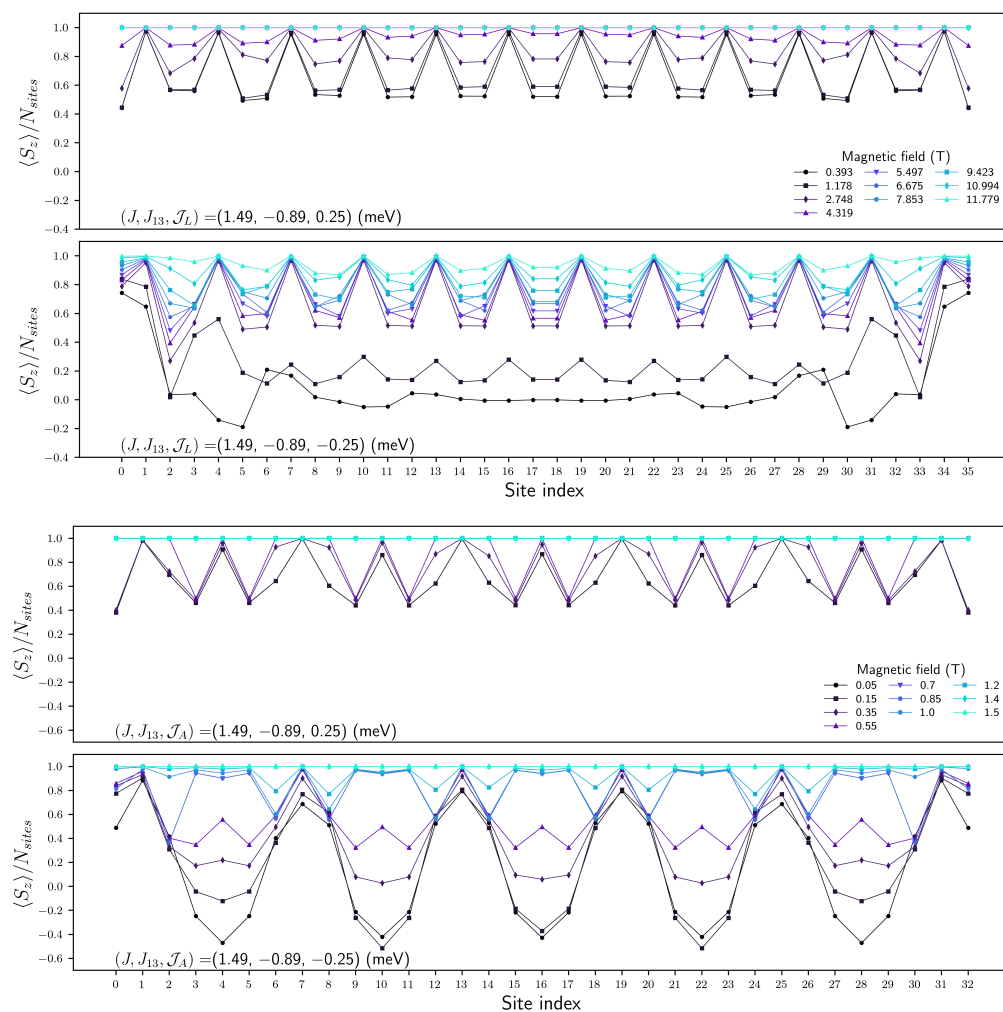


**Figure A6.** Local magnetizations for a 36 spin chain (12 3D SMMs) and  $\mathcal{J}_L = (0.25, -0.25)$  for upper two panels, respectively. Lower two panels have the local magnetizations for a 33 spin chain (11 3D SMMs) and  $\mathcal{J}_A = (0.25, -0.25)$ , respectively.

## References

- Carretta, S.; Zueco, D.; Chiesa, A.; Gómez-León, A.; Luis, F. A perspective on scaling up quantum computation with molecular spins. *Appl. Phys. Lett.* **2021**, *118*, 240501. [[CrossRef](#)]
- Zabala-Lekuona, A.; Seco, J.M.; Colacio, E. Single-Molecule Magnets: From Mn12-ac to dysprosium metallocenes, a travel in time. *Coord. Chem. Rev.* **2021**, *441*, 213984. [[CrossRef](#)]
- Florez, J.M.; Vargas, P. Factorizing magnetic fields triggered by the Dzyaloshinskii–Moriya interaction: Application to magnetic trimers. *J. Magn. Magn. Mater.* **2012**, *324*, 83–89. [[CrossRef](#)]
- Ghirri, A.; Troiani, F.; Affronte, M. Quantum Computation with Molecular Nanomagnets: Achievements, Challenges, and New Trends. In *Molecular Nanomagnets and Related Phenomena*; Gao, S., Ed.; Springer: Berlin/Heidelberg, Germany, 2015; pp. 383–430. [[CrossRef](#)]
- Blachowicz, T.; Ehrmann, A. New Materials and Effects in Molecular Nanomagnets. *Appl. Sci.* **2021**, *11*, 7510. [[CrossRef](#)]
- Islam, R.; Ma, R.; Preiss, P.M.; Eric Tai, M.; Lukin, A.; Rispoli, M.; Greiner, M. Measuring entanglement entropy in a quantum many-body system. *Nature* **2015**, *528*, 77–83. [[CrossRef](#)] [[PubMed](#)]
- Bazhanov, D.I.; Sivkov, I.N.; Stepanyuk, V.S. Engineering of entanglement and spin state transfer via quantum chains of atomic spins at large separations. *Sci. Rep.* **2018**, *8*, 14118. [[CrossRef](#)] [[PubMed](#)]
- Ferrando-Soria, J.; Moreno Pineda, E.; Chiesa, A.; Fernandez, A.; Magee, S.A.; Carretta, S.; Santini, P.; Vitorica-Yrezabal, I.J.; Tuna, F.; Timco, G.A.; et al. A modular design of molecular qubits to implement universal quantum gates. *Nat. Commun.* **2016**, *7*, 11377. [[CrossRef](#)] [[PubMed](#)]
- Wu, W.H.; Wang, Y.Q.; Mi, H.L.; Xue, Q.X.; Shao, F.; Shen, F.; Yang, F.L. Magnetic relaxation in a Co(II) chain complex: Synthesis, structure, and DFT computational coupling constant. *CrystEngComm* **2021**, *23*, 1398–1405. [[CrossRef](#)]

10. Montenegro-Filho, R.R.; Silva-Júnior, E.J.P.; Coutinho-Filho, M.D. Ground-state phase diagram and thermodynamics of coupled trimer chains. *Phys. Rev. B* **2022**, *105*, 134423. [[CrossRef](#)]
11. Sun, H.L.; Wang, Z.M.; Gao, S. Strategies towards single-chain magnets. *Coord. Chem. Rev.* **2010**, *254*, 1081–1100. [[CrossRef](#)]
12. Cheng, J.Q.; Li, J.; Xiong, Z.; Wu, H.Q.; Sandvik, A.W.; Yao, D.X. Fractional and Composite Excitations of Antiferromagnetic Quantum Spin Trimer Chains. *npj Quantum Mater.* **2022**, *7*, 3. [[CrossRef](#)]
13. Meng, X.; Shi, W.; Cheng, P. Magnetism in one-dimensional metal–nitronyl nitroxide radical system. *Coord. Chem. Rev.* **2019**, *378*, 134–150. [[CrossRef](#)]
14. Tin, P. Haldane topological spin-1 chains in a planar metal-organic framework. *Nat. Commun.* **2023**, *14*, 5454. [[CrossRef](#)] [[PubMed](#)]
15. Mellado, P. Intrinsic topological magnons in arrays of magnetic dipoles. *Sci. Rep.* **2022**, *12*, 1420. [[CrossRef](#)] [[PubMed](#)]
16. Pouget, J.P. Spin-Peierls, Spin-Ladder and Kondo Coupling in Weakly Localized Quasi-1D Molecular Systems: An Overview. *Magnetochemistry* **2023**, *9*, 57. [[CrossRef](#)]
17. Arian Zad, H.; Zoshki, A.; Ananikian, N.; Jaščur, M. Tomonaga-Luttinger Spin Liquid and Kosterlitz-Thouless Transition in the Spin-1/2 Branched Chains: The Study of Topological Phase Transition. *Materials* **2022**, *15*, 4183. [[CrossRef](#)] [[PubMed](#)]
18. Mashiko, T.; Nomura, K. Phase transition of an SU(3) symmetric spin-1 chain. *Phys. Rev. B* **2021**, *104*, 155405. [[CrossRef](#)]
19. Serwatka, T.; Melko, R.G.; Burkov, A.; Roy, P.N. Quantum Phase Transition in the One-Dimensional Water Chain. *Phys. Rev. Lett.* **2023**, *130*, 026201. [[CrossRef](#)]
20. Baiardi, A.; Reiher, M. The density matrix renormalization group in chemistry and molecular physics: Recent developments and new challenges. *J. Chem. Phys.* **2020**, *152*, 040903. [[CrossRef](#)]
21. Heveling, R.; Richter, J.; Schnack, J. Thermal density matrix renormalization group for highly frustrated quantum spin chains: A user perspective. *J. Magn. Magn. Mater.* **2019**, *487*, 165327. [[CrossRef](#)]
22. Kim, J.; Kim, M.; Kawashima, N.; Han, J.H.; Lee, H.Y. Construction of variational matrix product states for the Heisenberg spin-1 chain. *Phys. Rev. B* **2020**, *102*, 085117. [[CrossRef](#)]
23. Tilly, J.; Chen, H.; Cao, S.; Picozzi, D.; Setia, K.; Li, Y.; Grant, E.; Wossnig, L.; Rungger, I.; Booth, G.H.; et al. The Variational Quantum Eigensolver: A review of methods and best practices. *Phys. Rep.* **2022**, *986*, 1–128. [[CrossRef](#)]
24. Castro, A.; García Carrizo, A.; Roca, S.; Zueco, D.; Luis, F. Optimal Control of Molecular Spin Qudits. *Phys. Rev. Appl.* **2022**, *17*, 064028. [[CrossRef](#)]
25. Chizzini, M.; Crippa, L.; Chiesa, A.; Tacchino, F.; Petiziol, F.; Tavernelli, I.; Santini, P.; Carretta, S. Molecular nanomagnets with competing interactions as optimal units for qudit-based quantum computation. *Phys. Rev. Res.* **2022**, *4*, 043135. [[CrossRef](#)]
26. Domanov, O.; Weschke, E.; Saito, T.; Peterlik, H.; Pichler, T.; Eisterer, M.; Shiozawa, H. Exchange coupling in a frustrated trimetric molecular magnet reversed by a 1D nano-confinement. *Nanoscale* **2019**, *11*, 10615–10621. [[CrossRef](#)]
27. Bera, A.K.; Yusuf, S.M.; Saha, S.K.; Kumar, M.; Voneshen, D.; Skourski, Y.; Zvyagin, S.A. Emergent many-body composite excitations of interacting spin-1/2 trimers. *Nat. Commun.* **2022**, *13*, 6888. [[CrossRef](#)]
28. Zhang, J.; Deng, Y.; Hu, X.; Chi, X.; Liu, J.; Chu, W.; Sun, L. Molecular Magnets Based on Graphenes and Carbon Nanotubes. *Adv. Mater.* **2019**, *31*, 1804917. [[CrossRef](#)]
29. Villalva, J.; Develioglu, A.; Montenegro-Pohlhammer, N.; Sánchez-de Armas, R.; Gamonal, A.; Rial, E.; García-Hernández, M.; Ruiz-Gonzalez, L.; Costa, J.S.; Calzado, C.J.; et al. Spin-state-dependent electrical conductivity in single-walled carbon nanotubes encapsulating spin-crossover molecules. *Nat. Commun.* **2021**, *12*, 1578. [[CrossRef](#)]
30. Florez, J. M.; Núñez, Á.; García, C.; Vargas, P. Magnetocaloric features of complex molecular magnets: The Cr<sub>7</sub>Ni<sub>2</sub>Cu molecular magnet and beyond. *J. Magn. Magn. Mater.* **2010**, *322*, 2810–2818. [[CrossRef](#)]
31. Karl'ová, K.; Strečka, J.; Haniš, J.; Hagiwara, M. Insights into Nature of Magnetization Plateaus of a Nickel Complex [Ni<sub>4</sub>(μ-CO<sub>3</sub>)<sub>2</sub>(aetpy)<sub>8</sub>](ClO<sub>4</sub>)<sub>4</sub> from a Spin-1 Heisenberg Diamond Cluster. *Magnetochemistry* **2020**, *6*, 2312–7481. [[CrossRef](#)]
32. Park, K.; Yang, E.; Hendrickson, D. Electronic structure and magnetic anisotropy for nickel-based molecular magnets. *J. Appl. Phys.* **2005**, *97*, 10M522 [[CrossRef](#)]
33. Ghannadan, A.; Karl'ová, K.; Strečka, J. On the Concurrent Bipartite Entanglement of a Spin-1 Heisenberg Diamond Cluster Developed for Tetranuclear Nickel Complexes. *Magnetochemistry* **2022**, *8*, 156. [[CrossRef](#)]
34. Guo, F.; Bar, A.; Layfield, R. Main Group Chemistry at the Interface with Molecular Magnetism. *Chem. Rev.* **2019**, *119*, 8479–8505. [[CrossRef](#)]
35. Bogani, L.; Wernsdorfer, W. Molecular spintronics using single-molecule magnets. *Nat. Mater.* **2008**, *7*, 155405. [[CrossRef](#)]
36. Georgiev, M.; Chamati, H. Magnetization steps in the molecular magnet Ni<sub>4</sub>Mo<sub>12</sub> revealed by complex exchange bridges. *Phys. Rev.* **2020**, *101*, 094427. [[CrossRef](#)]
37. Florez, J.M.; Núñez, Á.S.; Vargas, P. Quenching points of dimeric single-molecule magnets: Exchange interaction effects. *J. Magn. Magn. Mater.* **2010**, *322*, 3623–3630. [[CrossRef](#)]
38. Soto, R.; Martínez, G.; Baibich, M.N.; Florez, J.M.; Vargas, P. Metastable states in the triangular-lattice Ising model studied by Monte Carlo simulations: Application to the spin-chain compound Ca<sub>3</sub>Co<sub>2</sub>O<sub>6</sub>. *Phys. Rev. B* **2009**, *79*, 657. [[CrossRef](#)]
39. Florez, J.M.; Vargas, P.; García, C.; Ross, C.A. Magnetic entropy change plateau in a geometrically frustrated layered system: FeCrAs-like iron-pnictide structure as a magnetocaloric prototype. *J. Phys.-Condens. Matter* **2013**, *25*, 226004. [[CrossRef](#)] [[PubMed](#)]
40. Florez, J.M.; Negrete, O.A.; Vargas, P.; Ross, C.A. Geometrically frustrated Fe<sub>2</sub>P-like systems: Beyond the Fe-trimer approximation. *J. Phys.-Condens. Matter* **2015**, *27*, 1–10. [[CrossRef](#)]

41. Ginsberg, A.P.; Martin, R.L.; Sherwood, R.C. Magnetic exchange in transition metal complexes. IV. Linear trimeric bis(acetylacetonato)nickel(II). *Inorg. Chem.* **1968**, *7*, 932–936. [[CrossRef](#)]
42. Krichevsky, D.M.; Shi, L.; Baturin, V.S.; Rybkovsky, D.V.; Wu, Y.; Fedotov, P.V.; Obratsova, E.D.; Kapralov, P.O.; Shilina, P.V.; Fung, K.; et al. Magnetic Nanoribbons with Embedded Cobalt Grown inside Single-Walled Carbon Nanotubes. *Nanoscale* **2022**, *14*, 1978–1989. [[CrossRef](#)]
43. Kambe, K. On the Paramagnetic Susceptibilities of Some Polynuclear Complex Salts. *J. Phys. Soc. Jpn.* **1950**, *5*, 48–51. [[CrossRef](#)]
44. Kharlamova, M.V.; Kramberger, C. Metallocene-Filled Single-Walled Carbon Nanotube Hybrids. *Nanomaterials* **2023**, *13*, 774. [[CrossRef](#)]
45. Schollwöck, U. The Density-Matrix Renormalization Group in the Age of Matrix Product States. *Ann. Phys.* **2011**, *326*, 96–192. [[CrossRef](#)]
46. Rausch, R.; Peschke, M.; Plorin, C.; Karrasch, C. Magnetic Properties of a Capped Kagome Molecule with 60 Quantum Spins. *SciPost Phys.* **2022**, *12*, 143. [[CrossRef](#)]
47. Souza, F.; Veríssimo, L.M.; Strečka, J.; Lyra, M.L.; Pereira, M.S.S. Exact and Density Matrix Renormalization Group Studies of Two Mixed Spin-(1/2,5/2, 1/2) Branched-Chain Models Developed for a Heterotrimetallic Fe-Mn-Cu Coordination Polymer. *Phys. Rev. B* **2020**, *102*, 064414. [[CrossRef](#)]
48. Haegeman, J.; Cirac, J.I.; Osborne, T.J.; Pižorn, I.; Verschelde, H.; Verstraete, F. Time-Dependent Variational Principle for Quantum Lattices. *Phys. Rev. Lett.* **2011**, *107*, 070601. [[CrossRef](#)] [[PubMed](#)]
49. Haegeman, J.; Lubich, C.; Oseledets, I.; Vandereycken, B.; Verstraete, F. Unifying Time Evolution and Optimization with Matrix Product States. *Phys. Rev. B* **2016**, *94*, 165116. [[CrossRef](#)]
50. Vidal, G. Efficient Simulation of One-Dimensional Quantum Many-Body Systems, Guifre Vidal. *Phys. Rev. Lett.* **2004**, *93*, 040502. [[CrossRef](#)]
51. Hauschild, J.; Pollmann, F. Efficient Numerical Simulations with Tensor Networks: Tensor Network Python (TeNPy). *SciPost Phys. Lect. Notes* **2018**, *5*. [[CrossRef](#)]
52. Um, J.; Park, H.; Hinrichsen, H. Entanglement versus mutual information in quantum spin chains. *J. Stat. Mech. Theory Exp.* **2012**, *2012*, P10026. [[CrossRef](#)]
53. Amico, L.; Fazio, R.; Osterloh, A.; Vedral, V. Entanglement in many-body systems. *Rev. Mod. Phys.* **2008**, *80*, 517–576. [[CrossRef](#)]
54. Scopa, S.; Calabrese, P.; Bastianello, A. Entanglement dynamics in confining spin chains. *Phys. Rev. B* **2022**, *105*, 125413. [[CrossRef](#)]
55. Wei, K.X.; Ramanathan, C.; Cappellaro, P. Exploring Localization in Nuclear Spin Chains. *Phys. Rev. Lett.* **2018**, *120*, 070501. [[CrossRef](#)]
56. Kam, C.F.; Chen, Y. Genuine Tripartite Entanglement as a Probe of Quantum Phase Transitions in a Spin-1 Heisenberg Chain with Single-Ion Anisotropy. *Ann. Phys.* **2022**, *534*, 2100342. [[CrossRef](#)]
57. Scheie, A.; Laurell, P.; Samarakoon, A.M.; Lake, B.; Nagler, S.E.; Granroth, G.E.; Okamoto, S.; Alvarez, G.; Tennant, D.A. Witnessing entanglement in quantum magnets using neutron scattering. *Phys. Rev. B* **2021**, *103*, 224434. [[CrossRef](#)]
58. Wootters, W.K. Entanglement of Formation of an Arbitrary State of Two Qubits. *Phys. Rev. Lett.* **1998**, *80*, 2245–2248. [[CrossRef](#)]
59. Saguia, A.; Sarandy, M.S.; Boechat, B.; Continentino, M.A. Entanglement entropy in random quantum spin-S chains. *Phys. Rev. A* **2007**, *75*, 052329. [[CrossRef](#)]

**Disclaimer/Publisher’s Note:** The statements, opinions and data contained in all publications are solely those of the individual author(s) and contributor(s) and not of MDPI and/or the editor(s). MDPI and/or the editor(s) disclaim responsibility for any injury to people or property resulting from any ideas, methods, instructions or products referred to in the content.